Downloaded from orbit.dtu.dk on: May 05, 2023

DTU Library

Meteorological observations in support of a hill cap cloud experiment

Nielsen, M.

Publication date:
1998

Document Version
Publisher's PDF, also known as Version of record

Link back to DTU Orbit

Citation (APA):
Nielsen, M. (1998). *Meteorological observations in support of a hill cap cloud experiment*. Denmark. Forskningscenter Risoe. Risoe-R No. 1032(EN)

General rights
Copyright and moral rights for the publications made accessible in the public portal are retained by the authors and/or other copyright owners and it is a condition of accessing publications that users recognise and abide by the legal requirements associated with these rights.

- Users may download and print one copy of any publication from the public portal for the purpose of private study or research.
- You may not further distribute the material or use it for any profit-making activity or commercial gain
- You may freely distribute the URL identifying the publication in the public portal

If you believe that this document breaches copyright please contact us providing details, and we will remove access to the work immediately and investigate your claim.

RISØ

DK9802600

Risø-R-1032(EN)

Meteorological Observations in Support of a Hill Cap Cloud Experiment

Morten Nielsen

MASTER

RECEIVED
OCT 05 1998
OSTI

DISTRIBUTION OF THIS DOCUMENT IS UNLIMITED
FOREIGN SALES PROHIBITED

Risø National Laboratory, Roskilde, Denmark
July 1998

DISCLAIMER

Portions of this document may be illegible in electronic image products. Images are produced from the best available original document.

Risø-R-1032(EN)

Meteorological Observations in Support of a Hill Cap Cloud Experiment

Morten Nielsen

Risø National Laboratory, Roskilde, Denmark
July 1998

Abstract Humid air flows form a hill cap cloud over theAgana mountain ridge in the northeast of Tenerife. The HILLCLOUD project utilised this cloud formation to investigate the chemical and physical properties of cloud aerosols by land based observations. The project was part of the second Aerosol Characterisation Experiment (ACE-2) of the International Global Atmospheric Chemistry project (IGAC). The present report describes meteorological observations in support of the hill cap cloud experiment. Time-series of wind speed, wind direction, temperature and humidity were collected at ground-based meteorological stations during a period starting one year in advance of the main campaign. A series of radiosondes detecting the upstream stability and wind profile were launched during the main campaign.

CEC Contract No. : ENV4–CT95–0058
Supported by the D.G. XII Environment and Climate Programme as part of the second Aerosol Characterisation Experiment (ACE-2).

ISBN 87–550–2364–9
ISSN 0106–2840

Information Service Department · Risø · 1998

Contents

1 Introduction *5*

2 Site descriptions *5*

3 Ground based measurements *10*
3.1 Reduced time series and flow statistics *10*
3.2 Detailed time series *16*
3.3 Flow classification *22*

4 Radiosonde measurements *23*

5 Conclusions *32*

Acknowledgement *33*

References *33*

A Parameters for radiosonde analysis *34*

B Two-dimensional flow model *37*

C Overview during intensive runs *38*

1 Introduction

ACE-2

This work is a contribution to the second aerosol characterisation experiment (ACE-2) which was carried out during the summer of 1997 in the North Atlantic area southeast of the Azores. The overall aim was to determine the chemical and physical processes which control atmospheric aerosols over the ocean. Contrary to ACE-1 that was located in an unpolluted area south of Tasmania, ACE-2 was situated in an area with occasional antropogenic pollution from Europe. Radiative forcing by added aerosols and enhanced cloud formation caused by an altered selection of condensation nuclei might affect the regional climate. The main campaign was held in the period from June 16 till July 24 1997, and a pre-campaign was held in July 1–26 1996. A general introduction to ACE-2 is found on the internet at `http://rea.ei.jrc.it/~vandinge/ace2/ace2main.html`

HILLCLOUD

HILLCLOUD was one of several projects within ACE-2 supported by the Commission of the European Community (CEC). It was led by the Department of Chemistry, University of Manchester Institute for Science and Technology (UMIST). The HILLCLOUD methodology was to utilise the hill cap cloud often situated over a mountain ridge in Tenerife to study aerosol processes by ground based measurements. These measurements were done at three stations in the incoming unsaturated air, inside the hill cap cloud at the summit of the mountain ridge and on the rear side of the mountain. Chemical and physical aerosol cloud processing is detected by comparative analysis of data from the three sites. This technique was previously applied in the Great Dunn Fell (UK) experiments, as described by Chandler et al (1988), Gallagher et al (1990) and Choularton et al (1992).

Risø's role

Risø's role was to measure and characterize the flow over the mountain. Meteorological stations were established near each of the HILLCLOUD measuring sites. They collected data for a period including both the 1996 pre-campaign and the main ACE-2 campaign. The prime purpose was to document whether the flow came from the preferred direction transporting the air undisturbed over the mountain during runs of intensive aerosol sampling by our project partners. In addition, we chosed to monitor the flow for a one-year period in order to investigate the local meteorology. Based on these measurements we learned that sometimes the flow separated from the sharp mountain ridge and reversed at ground level on the rear side of the mountain. In other cases the wind was unusually strong on the rear side – probably because of lee waves induced by atmospheric stratification. In case of clear sky and weak synoptic wind, radiative cooling created local katabatic flows.

collaborations

The HILLCLOUD project interacts with other ACE-2 projects, in particular with FREETROPE which also involved ground-based measurements on Tenerife. The analysis in the present report includes meteorological measurements by the Environmetal Institute of the CEC Joint Research Centre (JRC) at Ispra. JRC operated a similar meteorological station on the northern coast and launched a series of radiosondes during the main ACE-2 campaign.

2 Site descriptions

The Island

Tenerife (ES), the largest of the Canary Islands, is located at 28°N, 16 °W in the North Atlantic ocean west of North Africa. The shape of Tenerife is a cone with the 3716-m high vulcano Teide at its centre. The Anaga peninsula to the NE of the island has a 700-m high mountain ridge with an ENE-WSW axis, see figure 1. The prevailing regional synoptic flow is the trade wind coming from directions centred

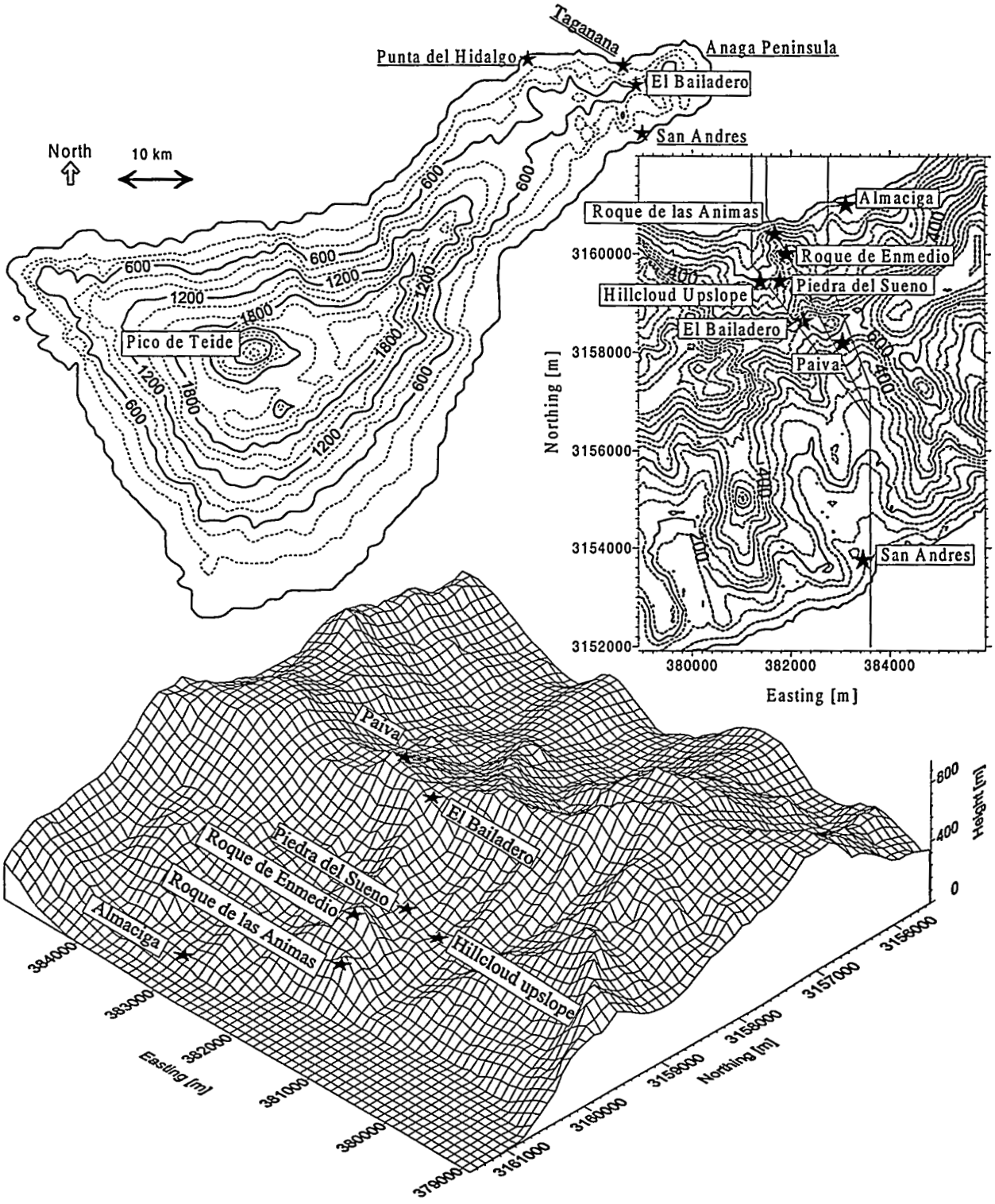

Figure 1. Map of Tenerife with close-up of the HILLCLOUD area and a perspective of the Taganana valley seen from NW at a tilt angle of 35°. The height scale of the perspective is enlarged by a factor of two relative to the horizontal scales.

at NE. The meteorology group at Universite Blaise Pascal, Clermont Ferrand (F), a sub-contractor to UMIST, previously simulated typical flow situations by a non-hydrostatic meso-scale model (Troude 1996). The meso-scale model predicted the lower troposphere to be forced almost perpendicular across the Anaga peninsula in case of synotic flows from N or NE. Sometimes a baroclinic downdraught forms

on the rear side of the mountain. The maritime air mass is usually quite moist, and the adiabatic cooling associated with the passage of the mountain ridge often results in a hill cap cloud.

The HILLCLOUD area

The HILLCLOUD aerosol measurements were made up at three stations across the Anaga ridge during the main ACE-2 campaign and the 1996 pre-campaign. These locations were, see figure 1,

1. the Taganana valley north of the ridge (HILLCLOUD upslope site)
2. the pass (El Bailadero)
3. the San Andres valley south of the ridge (Paiva).

UMIST visited the area and arranged tenancies inside buildings (a village house, a restaurant, and a cottage) with access to power and sufficient room for equipment. These buildings were used during the 1996 pre-campaign, but in the main ACE-2 campaign it was found necessary also to hire containers and scaffoldings which were arranged for better aerosol sampling. The 3D view inserted at the bottom of figure 1 gives an impression of the topography. The valleys are formed by erosion and have normally dried-up creeks (barrancos) at their bottom. Taganana valley has several such creeks which assemble into one before reaching the sea. The measurements took place in the eastern branch of Taganana valley leading to the pass at El Bailadero. This pass is 675 m above sea level and the distance to the valley inlet at the coast is 2 km. The last 100-m elevation to the summit has an impressive average slope angle of 55°! The 450-m hill Roques de Enmedio and the 382-m Roque de las Animas separate the Taganana valley from that of Almaciga to the east. Toward the south San Andres valley is 4.5 km long and therefore not as steep as Taganana valley. Figure 2 shows the terrain profiles along the Taganana and Almaciga valleys, over the separating hills and an average profile.

meteorological stations

Risø visited the island in February 1996, located the HILLCLOUD sites and decided to establish meteorological stations on masts close to the rented buildings at El Bailadero and Paiva. The main purpose of the meteorological stations was to provide information on the air flow during the aerosol measuring campaigns. In addition the stations were continuously running in the period between these campaigns.

Piedra de Sueno

The HILLCLOUD upslope site in Taganana valley was not found suitable for meteorological measurements, since nearby buildings and terrain were expected significantly to affect local wind speed and direction. Therefore an alternative site was found 400 m away at Piedra del Sueno near the footpath on top of a low ridge between two 'barrancos' with a NNW-SSE axis. The vegetation height on the Piedra del Sueno ridge is about 0.3 m.

El Bailadero

El Bailadero is situated on the summit at a place where a road approaches the steep northern slope. The restaurant rented by the HILLCLOUD project has a good view of Taganana valley, but apart from a nearby 50-m stretch of road the surrounding area is covered by trees and bushes. It was difficult to find a mast position in these surroundings and therefore it was decided to mount the meteorological equipment on a permanent tower owned by a television transmission company (Retevisión). This tower is close to the edge and the meteorological instruments were well-exposed to the wind.

Paiva

The area immediately south of El Bailadero is also covered with vigorous vegetation of considerable height. Therefore the HILLCLOUD downslope site was placed in a neighbouring branch of San Andres valley towards the east, see figure 1. It is possible that the flow at Paiva sometimes arrived from the pass to the Almagica valley. This pass has the same altitude as that of El Bailadero pass with a similar along-valley cross section, see figure 2. The cloud processing should therefore be identical and apart from cases of local polutions, the Paiva aerosol measurements

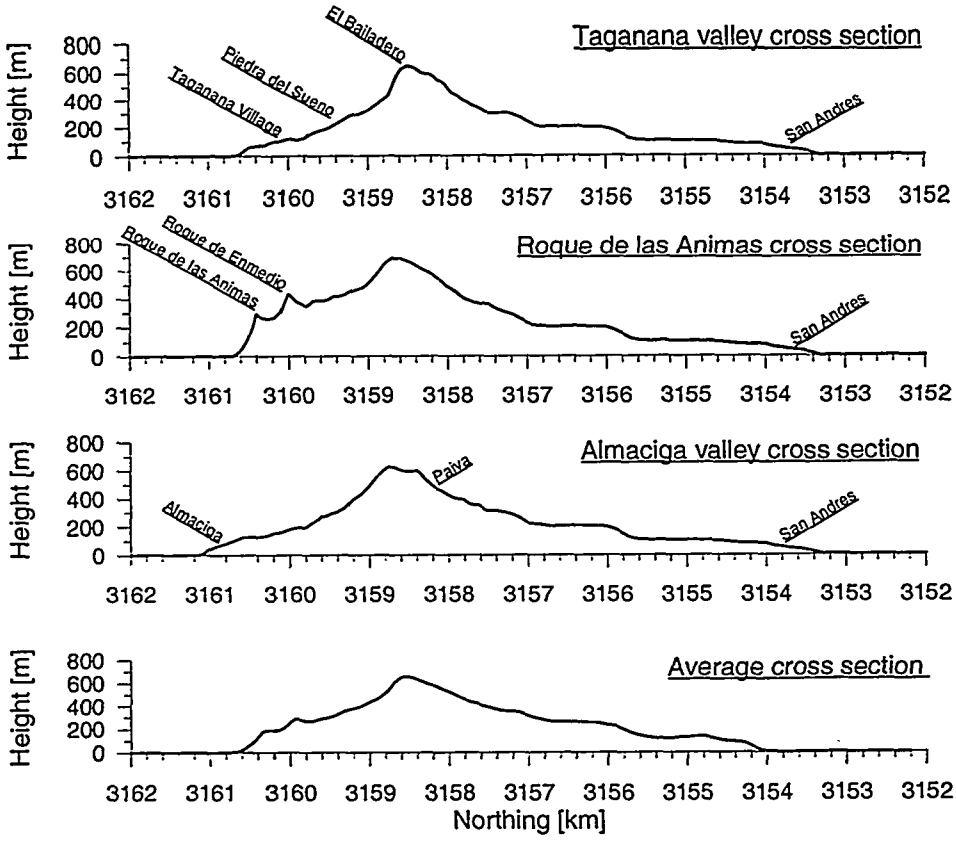

Figure 2. Three terrain profiles along the paths indicated on the top-right map of figure 1 plus a profile averaged over a 10-km wide corridor with a NNW-SSE axis centred at El Bailadero.

should be compatible with those from the other stations. The met-mast was placed on a terrace of an abandoned clay-pigeon shooting club without bushes. The flow was probably affected by a knoll 40-m above local terrain just 100 m west of the mast.

Punta del Hidalgo

The Joint Research Centre (JRC) operated a similar meteorological station 11 km west of Taganana on top of the lighthouse at Punta del Hidalgo. The area around the lighthouse is flat and the flow is representative of coastal winds. According to Troude (1996) these coastal winds are affected however by partial blocking of the tall island.

The measuring positions are listed in table 1. The universal tranverse mercator projection (UTM) is an orthogonal coordinate system with units in km.

Table 1. Measuring positions in geographic coordinates, UTM 28 [km×km], terrain altitude [m], and measuring level above terrain [m].

Site	Geographical coordinates	UTM 28 coordinates	Alt.	Lev.	Description
Punta del Hidalgo	(28°34'29.1"N, 16°19'36.0"W)	(E 370.245, N 3161.635)	5	55	lighthouse
HILLCLOUD upslope	(28°33'21.3"N, 16°12'45.6"W)	(E 381.375, N 3159.430)	220	–	house
Piedra del Sueno	(28°33'21.9"N, 16°12'31.1"W)	(E 381.770, N 3159.445)	310	7	mast on ridge
El Bailadero	(28°32'55.4"N, 16°12'13.1"W)	(E 382.250, N 3158.625)	675	6	television mast
Paiva	(28°32'41.7"N, 16°11'44.1"W)	(E 383.035, N 3158.195)	535	10	mast on terrace

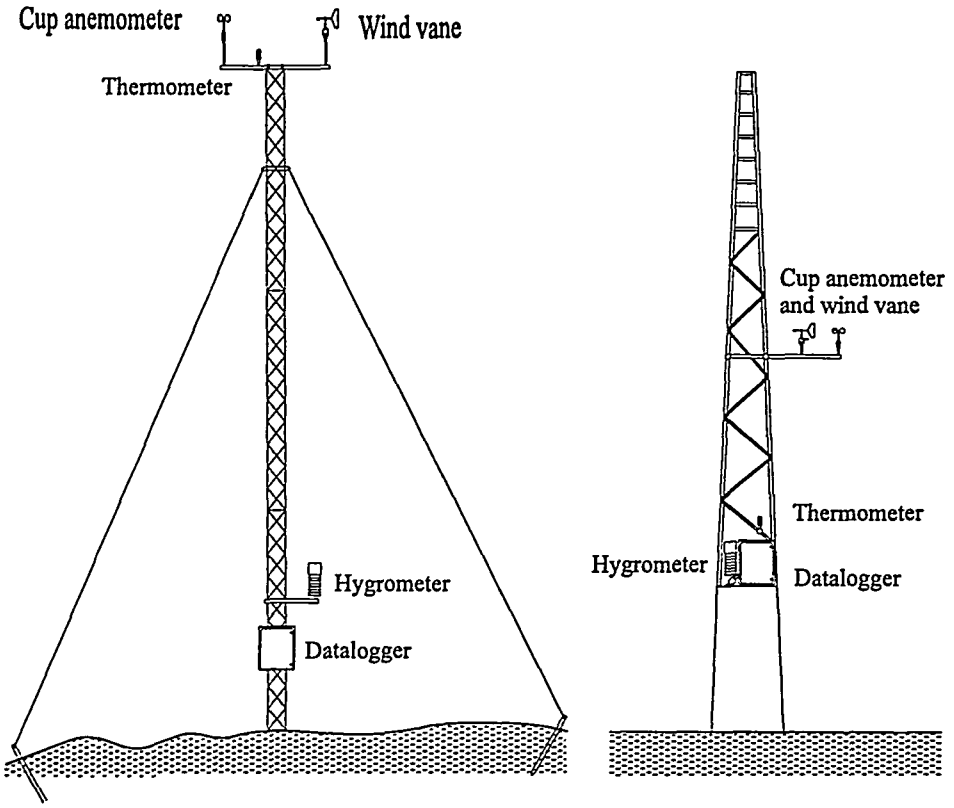

Figure 3. The temporary meteorological mast at Paiva and instrumentation of the permanent television transmission tower at El Baladero.

Meteorological stations

Figure 3 shows the Risø masts erected at Piedra del Sueno and Paiva and instrumentation of the permanent tele-transmission mast at El Bailadero. Each mast was equipped with a cup anemometer, a wind vane, a thermometer and a hygrometer. The station at Piedra del Sueno had an additional pyranometer for detection of solar radiation. The signals were collected on battery powered Vaisala dataloggers with exchangable data storage units. The dataloggers averaged the wind speed by summation of anemometer rotations during each sampling period. The wind direction and temperature sensors were artificially damped in order to achieve a response time matching the sampling period. The data storage units were renewed every second month and returned by mail for data extraction and quality control at Risø.

Digital maps

The meteorology group at Universite Blaise Pascal kindly provided a set of (X, Y, Z) coordinates digitised from the terrain contours of the 1:100.000, Mapa Guia, Direccion General del Instituto Geografico Nacional, covering all of Tenerife. This terrain model was originally applied in the meso-scale flow simulations mentioned above (Troude 1996). Risø produced similar supplementary terrain coordinates of Taganana Valley from the 1:25.000 Mapa General 5V, Cartografía Militara de España, ie with four times better precission in a limited area. An estimated 0.5-mm horizontal precision during the digitalisation process correspods to physical-scale precisions of ±100 m for the Tenerife map and ±25 m for the local Taganana map. The digitalization techniques were to trace selected contour lines producing the chains of data points shown in figure 4. For practical purposes, eg numer-

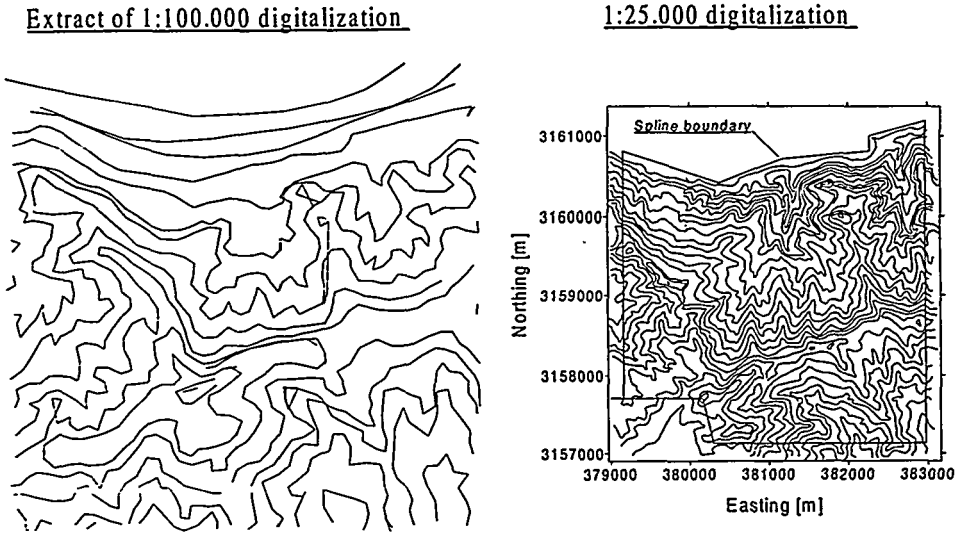

Figure 4. Terrain data points digitised from the 1:100.000 map (Clermont Ferrand) and the 1:25.000 map (Risø). A spline boundary to merge the topological data sets is indicated on the high-resolution map.

ical modeling, it is more convenient to work with a terrain model of the form $Z = f(X,Y)$ where the horizontal coordinates X and Y are organised in an orthogonal grid with equidistant separations. Such interpolated files are obtained by interpolation between the irregularly distributed contour data. It is appropriate to apply the high-resolution data within the domain of Taganana valley and the low-resolution data in the far field. A combined terrain model is produced by the following weighting function:

$$Z = \alpha f_1(X,Y) + (1-\alpha) f_2(X,Y)$$

The f_1 and f_2 functions are the two digital maps and α is a smooth spline function defined by

$$\alpha = \begin{cases} 1 & \text{within the high-resolution domain, } \delta x \le -l \\ \frac{1}{2}(1+\sin\frac{\pi\delta x}{2l}) & \text{in the transition zone, } -l < \delta x \le l \\ 0 & \text{outside the high-resolution domain, } \delta x > l \end{cases}$$

where δx is distance in the normal direction of the boundary surrounding the high-resolution domain, and $2l$ is width of the transition zone, eg $2l = 250$m.

3 Ground based measurements

This chapter is initiated by an overview of the available meteorological time series, followed by discussion of detailed time series and identification of typical flows. Overviews of flow conditions during HILLCLOUD intensive runs are given in Appendix C.

3.1 Reduced time series and flow statistics

The time series in figures 5 to 8 show daily average values of wind speed and direction; daily extreme values of temperature and relative humidity and daily maximum of solar radiation.

The following interruptions are identified: *missing data*

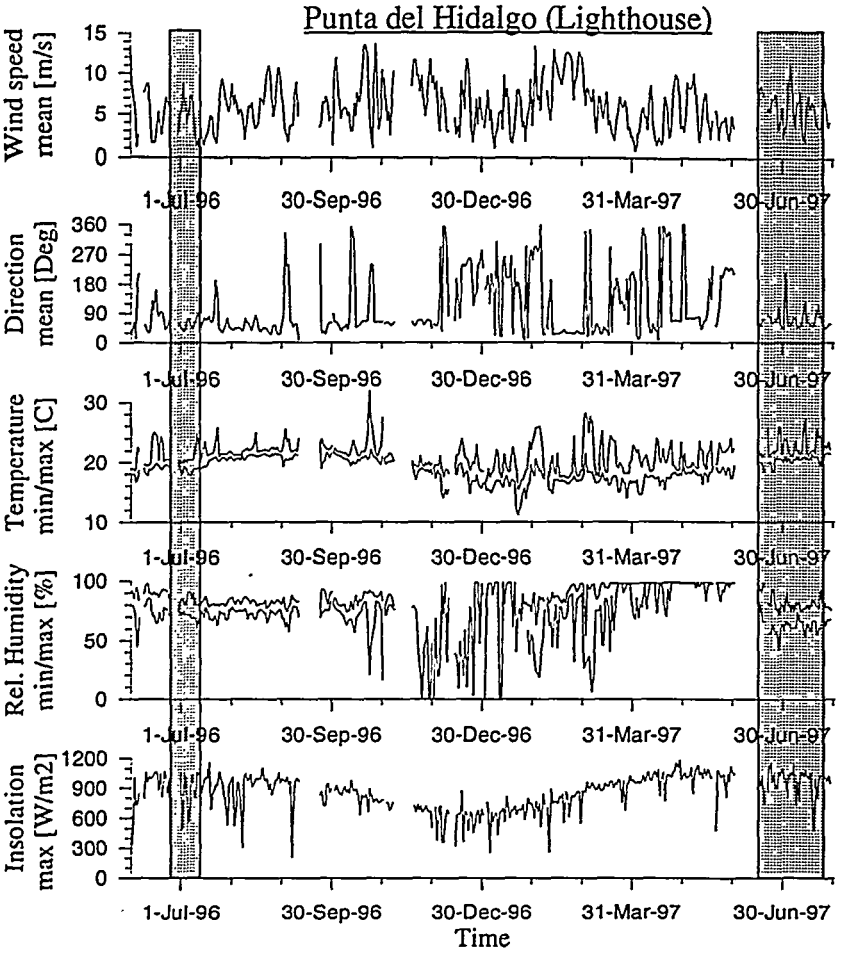

Figure 5. Selected daily statistics of measurements from Punta del Hidalgo (lighthouse): Average values of wind speed and direction, minimum and maximum of daily temperatures and relative humidity and maximum solar radiation. The shaded areas indicate the 1996 pre-campaign and the main ACE-2 campaign in 1997.

1. intermittent stops at Punta del Hidalgo;
2. intermittent stops at El Bailadero during start of the measurements;
3. a global stop at all Riso stations in the first week of September 1996;
4. missing wind direction data from Piedra del Suenno from September 1996 till January 1997.

The initial frequent interruptions at El Bailadero were caused by the datalogger which for some unknown reason seemed to trigger too often. This implied the datalogger to lose its timing. The problem persisted after replacement of the unit in January 1997 although it helped considerably to isolate all equipment from the television mast. In some cases the extra scans were manually removed[1], but it was impossible to recover data in case of very frequent interruptions. Unfortunately this caused loss of data during the 1996 pre-campaign. The reason for the global stop in September 1996 was a delay in the postal service which made it impossible for our local assistant to exchange the data storage units. The reason for the missing wind direction data from Piedra del Sueno is a stroke of lightning which damaged the sensor during a storm in September 1996. The instrument was

[1]The actual time was logged only at midnight and the timing of the remaining data were deduced from the scan numbers.

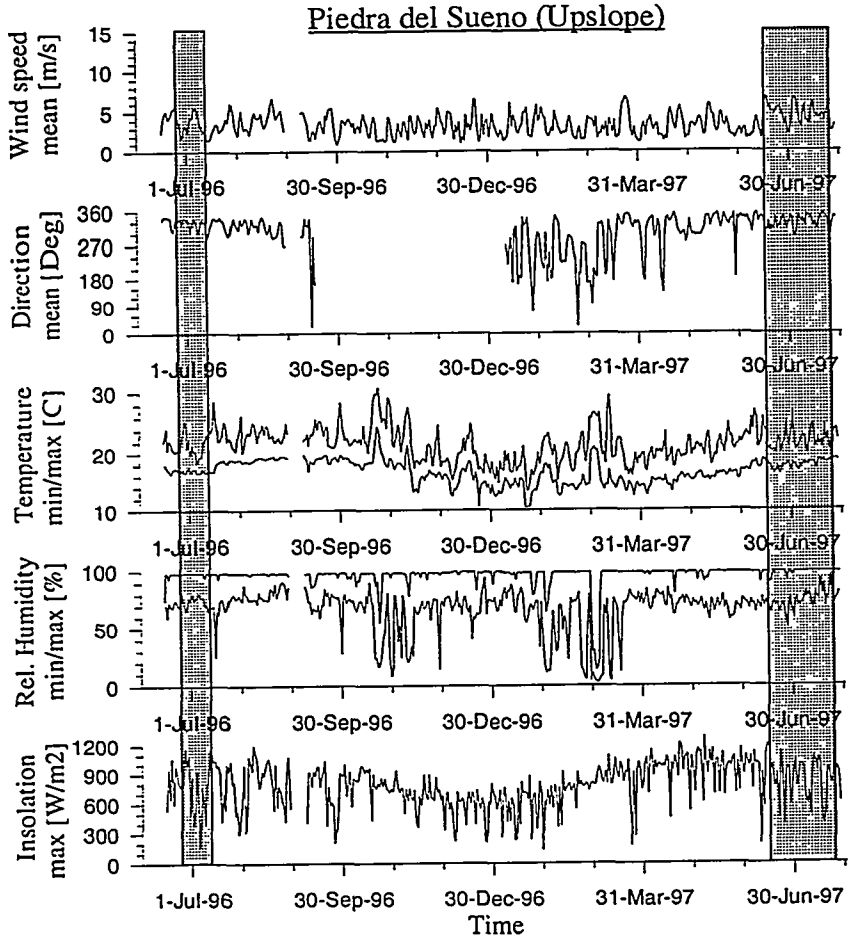

Figure 6. Selected daily statistics of measurements from Piedra del Sueno in Taganana Valley (upslope site), as in figure 5.

replaced in January 97. Fortunately no data are missing from the main ACE-2 campaign.

wind speed distributions

By comparison of the top frames of figures 5 to 8 it is seen that the wind speed was higher at the coastal and summit sites than in the valleys. The local wind-speed dependence on the observation level may be estimated by a logarithmic velocity profile:

$$u = \frac{u_*}{\kappa} \ln \frac{z}{z_0}$$

where u_* is the friction velocity, $\kappa = 0.4$ is the von Kármán constant and z_0 is the roughness length. The ratio between wind speed on top of the Punta del Hidalgo lighthouse and at a height comparable to the other measurements is

$$\frac{u_{10m}}{u_{55m}} \approx \begin{cases} 0.92 & \text{with } z_0 = 0.018\,u_*^2/g \text{ for onshore winds} \\ 0.77 & \text{with } z_0 = 0.05 \text{ for offshore winds} \end{cases}$$

Here the roughness length over sea is evaluated by the empirical Charnock's relation using the average wind speed of the Punta del Hidalgo observations. Thus the elevation of the Punta del Hidalgo measurements only explains 10-20% of the wind speeds increase - the open terrain accounts for the remaining difference. The wind tended to speed up during the passage of the mountain ridge and at El Bailadero and Paiva there seemed to be a tendency for higher wind speeds in summer. This tendency was not observed at the coastal site and might have been

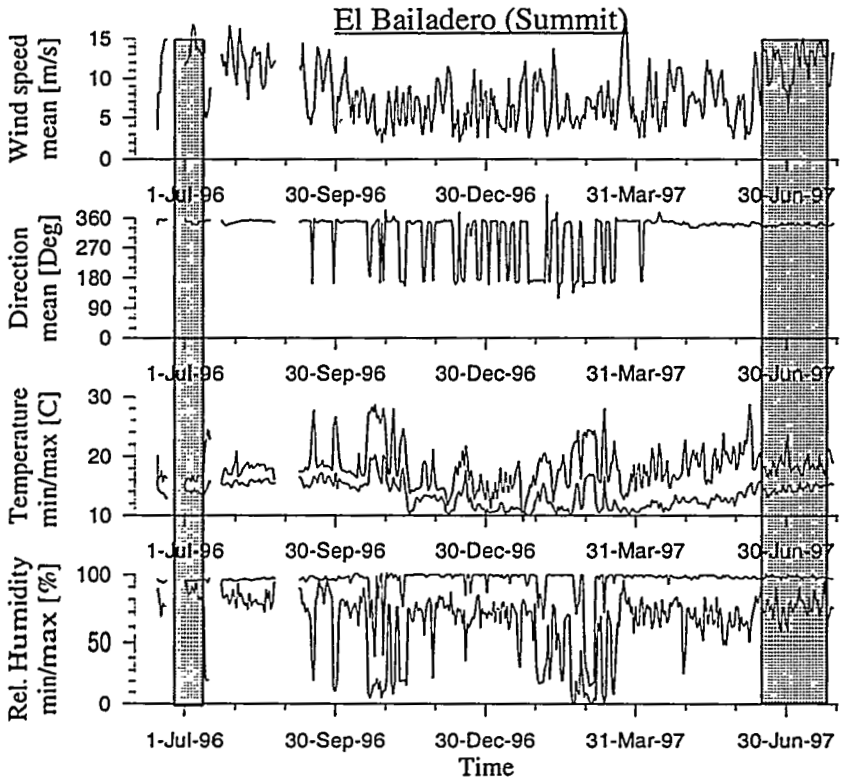

Figure 7. Selected daily statistics of measurements from El Bailadero (summit site), as in figure 5.

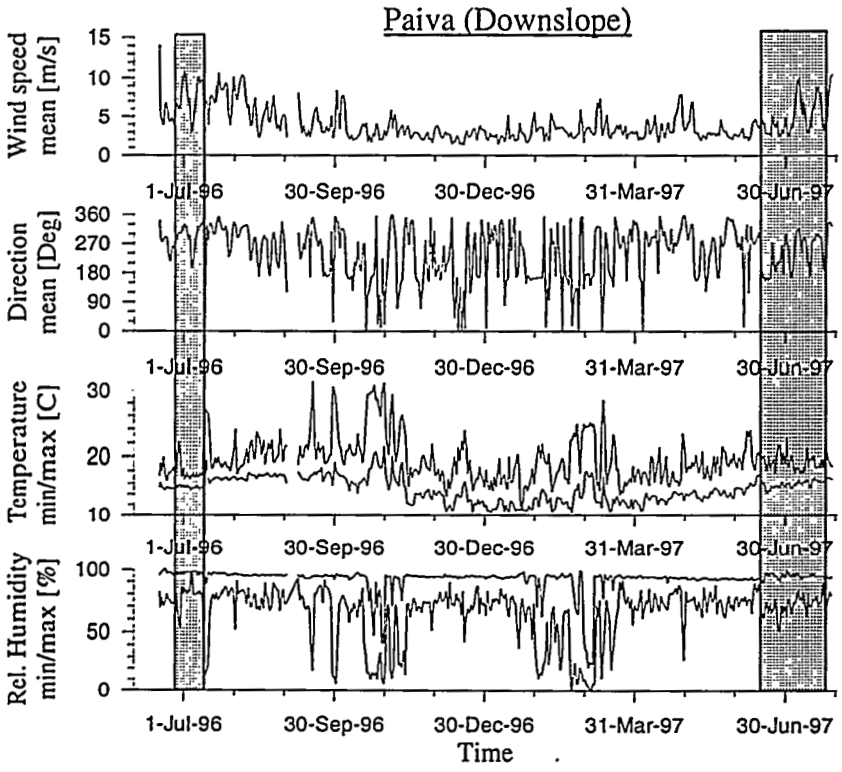

Figure 8. Selected daily statistics of measurements from Paiva in San Andres valley (downslope site), as in figure 5.

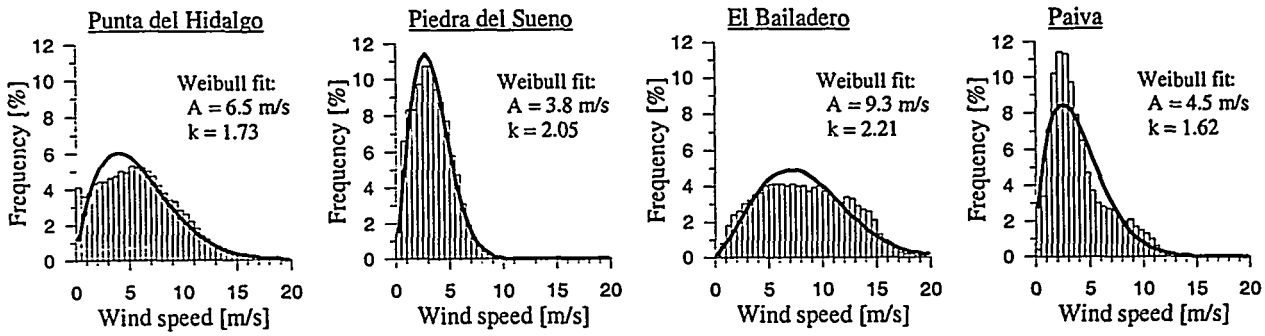

Figure 9. Wind speed distributions in bins with increments of 0.5 m/s and corresponding fits of Weibull distributions.

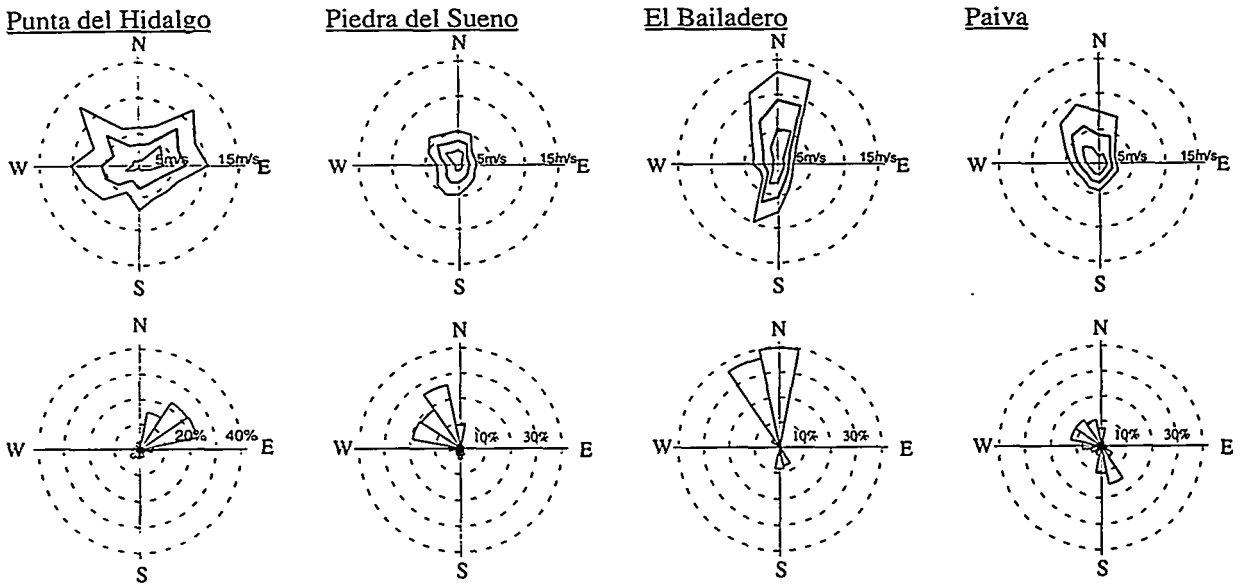

Figure 10. For each measuring station: 1) Average wind speed plus/minus one standard deviation depending on direction and 2) sector-wise frequency distributions.

caused by seasonal variation of the atmospheric stability. Figure 9 shows frequency distributions of the wind and fits of the often used Weibull distribution

$$P\{U \leq u\} = \exp\left\{-\left(\frac{u}{A}\right)^k\right\}$$

where A is a scale parameter and k is a shape parameter. The average wind speed is weakest at Piedra del Sueno and strongest at El Bailadero.

directional wind distributions

Wind direction signals are plotted in the second row of figures 5 to 8. The reader should be aware that some abrupt changes are caused by the cyclic horizontal direction which implies that 0° as well as 360° refer to northerly directions. Even with this in mind the wind direction signals appear quite different at the four sites. This is perhaps better illustrated by the sector-wise wind frequency distributions (wind roses) shown in the bottom row of figure 10. In these plots the winds are sorted in 16 sectors of $22\frac{1}{2}°$ angles centred around north (N), north-northeast (NNE), etc. The coastal wind at Punta del Hidalgo came most frequently from NE whereas the dominating wind direction at El Bailadero was N to NNW, as predicted by Troude (1996). El Bailadero winds from the exact opposite direction were also observed. The reason for this narrow wind rose was that the pressure gradients accelerated the flow in directions perpendicular to the mountain ridge. Going back to figure 7, it is seen that winds coming from the

south (reverse flows from a HILLCLOUD point of view) were most frequent in the winter. The winds at Piedra del Sueno had a broader distribution[2] centred around the local valley orientation which is slightly north of NW or 90° clockwise off the coastal wind. This is a terrain-induced effect. Winds straight from north were unexpected since this site was sheltered by the 450-m hill Roque de Enmedio east of the Taganana valley entrance, see figure 1. The wind direction was less predictable at Paiva than at the other sites. The preferred downslope direction was slightly west of NW whereas the preferred reverse direction was SSE, ie ≈30° off the opposite direction. Downslope flows had a tendency to dive into the gorge (Barranco de Piedra Grande) east of the Paiva site.

The plots in the top row of figure 10 show the average wind speeds and the average plus/minus one standard deviation as a function of local wind direction. These plots should be interpreted in connection with the frequencies below, eg it should be remembered that the exceptionally strong NW wind speeds at Punta del Hidalgo were observed only in a small fraction of the time. Apart from this sector, the strongest winds at Punta del Hidalgo were those blowing along the coast, in particular the easterly winds. The winds at Piedra del Sueno were relatively weak. The directional dependence was not very significant at this site although NW winds coming up the valley and southerly winds[3] tended to be the strongest ones. The winds at El Bailadero clearly speed up in the directions across the ridge with the strongest winds centred around N. The strongest winds at Paiva were the downslope winds centred around NW. The frequent southerly winds were weaker.

conditional wind distributions

Figure 11 and 12 are similar to figure 10 except that they are based on situations with either northerly or southerly winds at El Bailadero. By comparison of the plots in the top row of these figures it is observed that generally the speed of northerly winds was higher at Paiva than at Piedra del Sueno, whereas the oposite was true for southerly winds. In other words: the wind tends to speed up on the rear side of the mountain ridge, and this indicates the presence of occasional baroclinic downdraughts as predicted by Troude (1996). The wind roses at the bottom row of the figures were more scattered on the lee side of the mountain indicating some situations with flow reversal.

temperature & humidity

The temperature signals in the third frame of figures 5 to 8 had large excursions during winter. This is probably both because the wind came more frequently from south and because low wind speeds during winter provided more opportunities for local radiative heating or cooling. The relative humidities shown below are counter-correlated with the daytime temperatures[4] whereas the humidity goes into saturation nearly every night. Warm spells with southerly winds in winter are associated with very low humidities. Figure 13 examines the differences between daily extreme temperatures observed at the three stations in the HILLCLOUD area. The dashed lines indicate expected differences corresponding to a lapse rate of ≈ 0.01°C/m. With this correction the minimum temperatures are not very different at the three sites. During the summer the daily maxima tend to be highest at Piedra del Sueno whereas the opposite is true in winter. By comparison of figures 5 and 6 it is noted that the daily temperature and humidity ranges were smaller at the generally upstream coastal site. This indicates some radiative heating or cooling in the valleys.

insolation

The insolation was measured at Punta del Hidalgo and Piedra del Sueno. The envelope on these time series is a nearly sinusoidal variation with extreme values at summer and winter solstice. Observations lower than this envelope indicate local

[2]The presented wind rose from Piedra del Sueno is affected by missing autumn data and therefore not fully compatible with the other ones.

[3]Again based on relatively few observations

[4]In most cases the daily extremes are a temperature *maximum* and a relative humidity *minimum*.

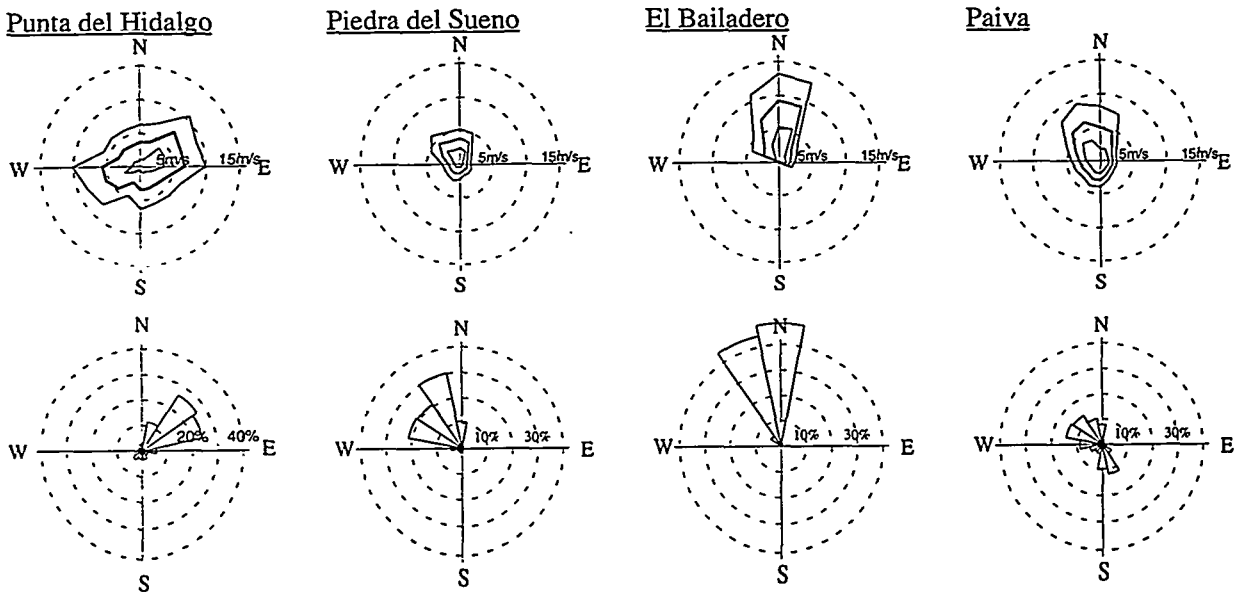

Figure 11. As figure 10, for northerly El Bailadero winds only.

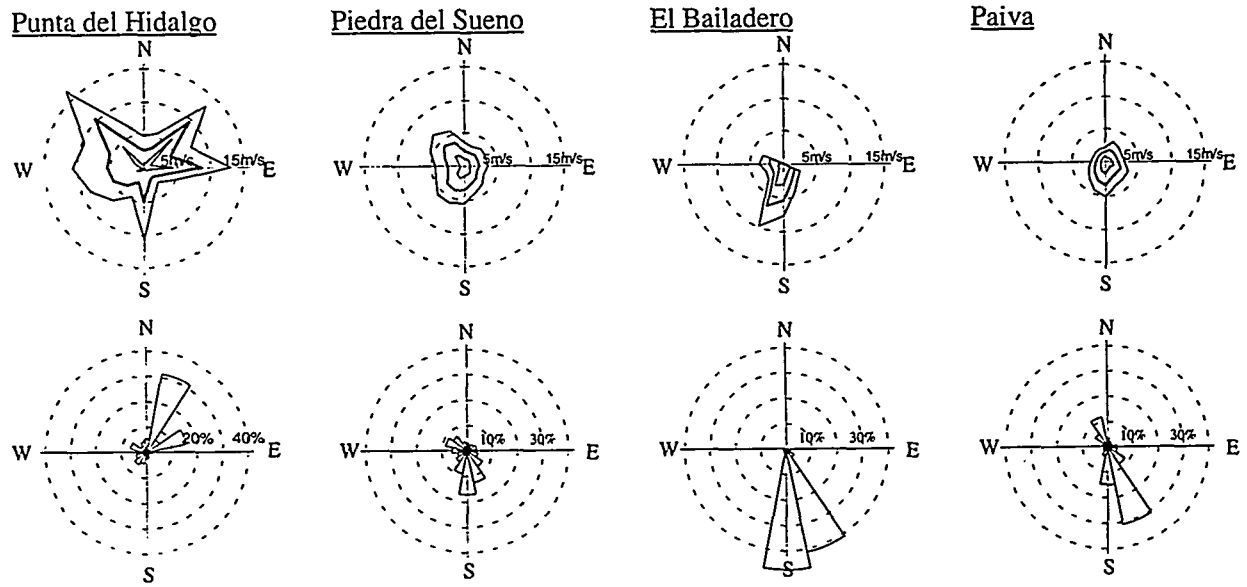

Figure 12. As figure 10, for southerly El Bailadero winds only (reverse flow).

clouds near noon. This seemed to happen more frequently at Piedra del Sueno than at the coastal site.

3.2 Detailed time series

Figures 14 to 17 shows detailed time series from the months with field campaigns. The latter figure is of primary interest because it includes eight HILLCLOUD intensive runs during the main ACE-2 campaign indicated by shades of gray. The following observations are made:

- The wind speed signals are rather different at the four sites. The main reason is probably terrain effects. *wind speed*
- In interpreting the wind direction time series is should be noted that the scale is cyclic, ie both 0° and 360° refer to northerly directions. Thus the costal *wind direction*

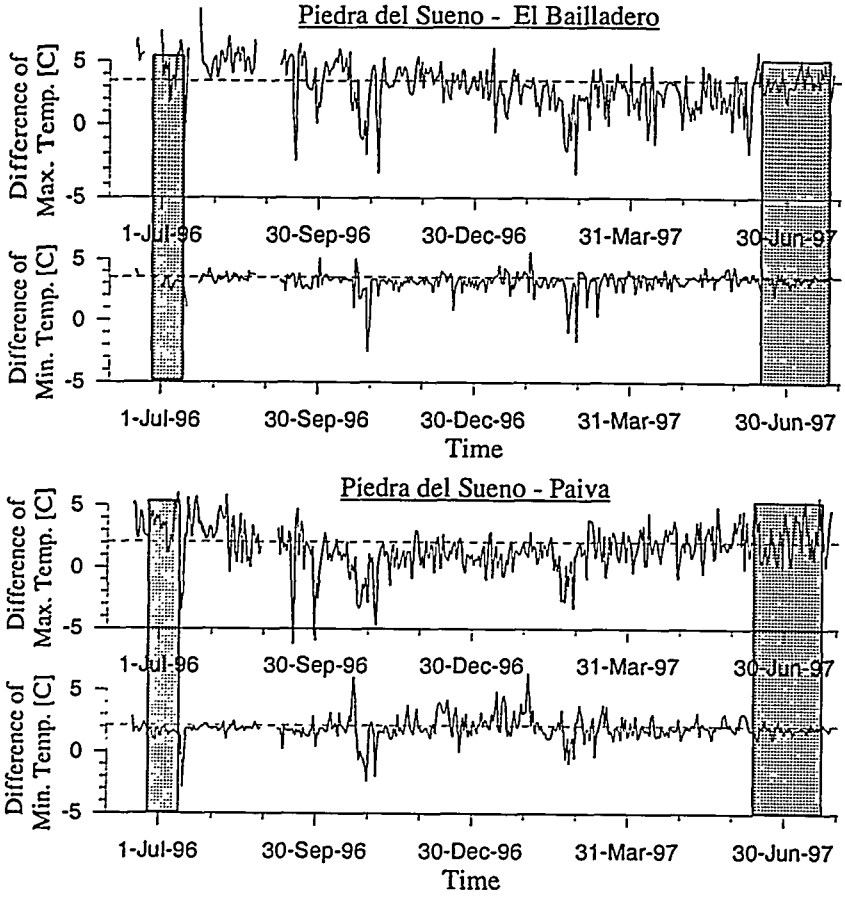

Figure 13. Temperature differences.

wind direction observed at Punta del Hidalgo was more stable than it may appear at first sight. The wind direction was steady also at Piedra del Sueno and in particular at El Bailadero where it deviated little from north during the entire month. Sometimes the wind direction at Paiva was observed to alternate intermittently between the preferred NW and S directions, eg on 16 June 1997. The local wind speed suddenly weakened during periods of flow reversal indicating that the cause was flow separation from the mountain ridge.

- Generally the solar radiation signal was weaker at Piedra del Sueno than at Punta del Hidalgo indicating more clouds in Taganana valley. *insolation*
- The temperature was more stable at Punta del Hidalgo than at the inland sites. It also seems like temperature excursions were slightly larger on the upslope and summit sites than at Paiva. *temperature*
- The relative humidity signals were countercorrelated with the temperature signals. This implies that absolute humidity was more steady than relative humidity. The relative humidity increases with altitude where it reaches saturation almost every night. Some relative humidity signals are 'clipped' at a level less than 100%. This is just a sensor problem and the air was probably saturated during these events. *humidity*

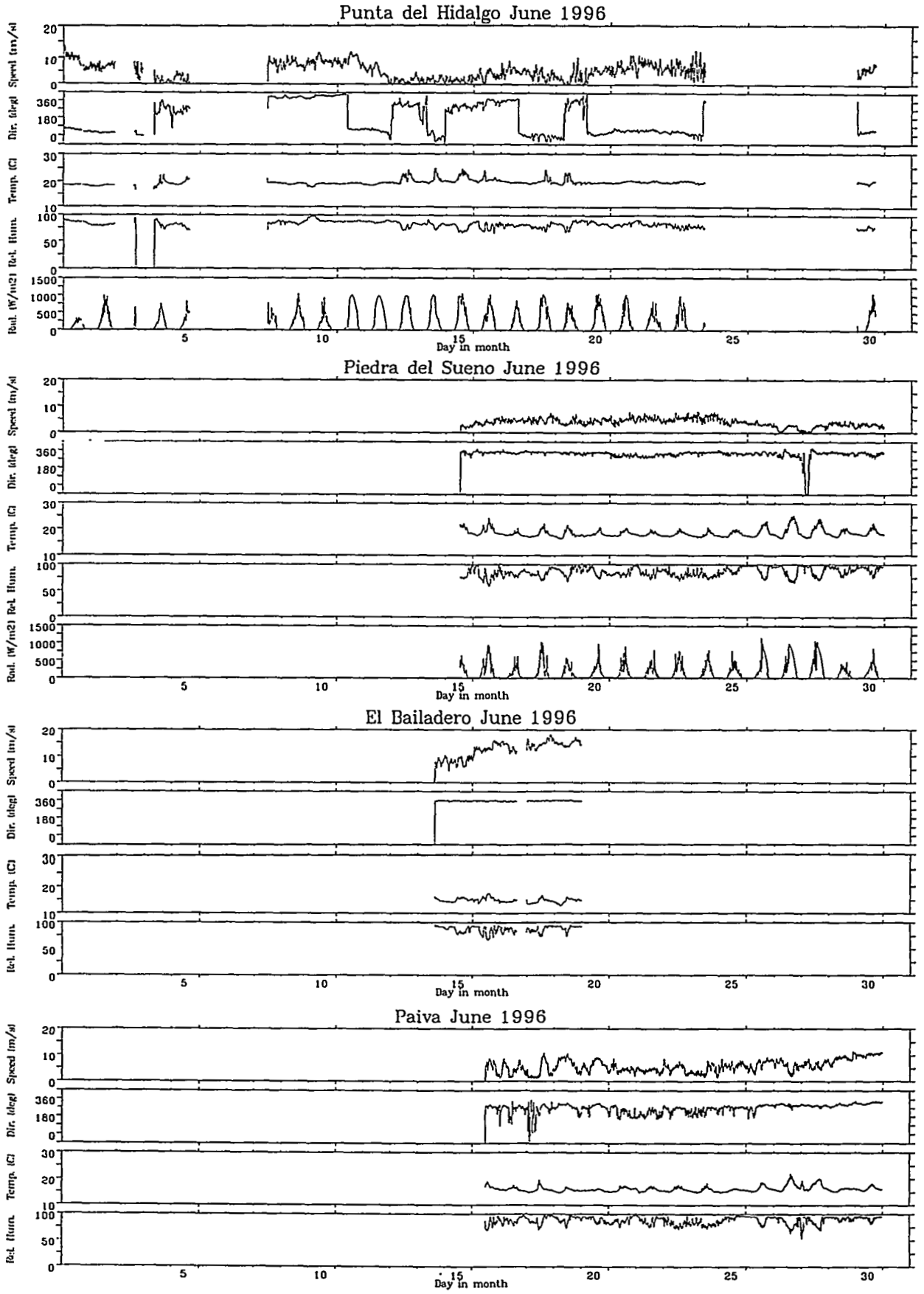

Figure 14. Time series of meteorological measurements in June 1996. The ACE-2 pre-campaign started on 24/6.

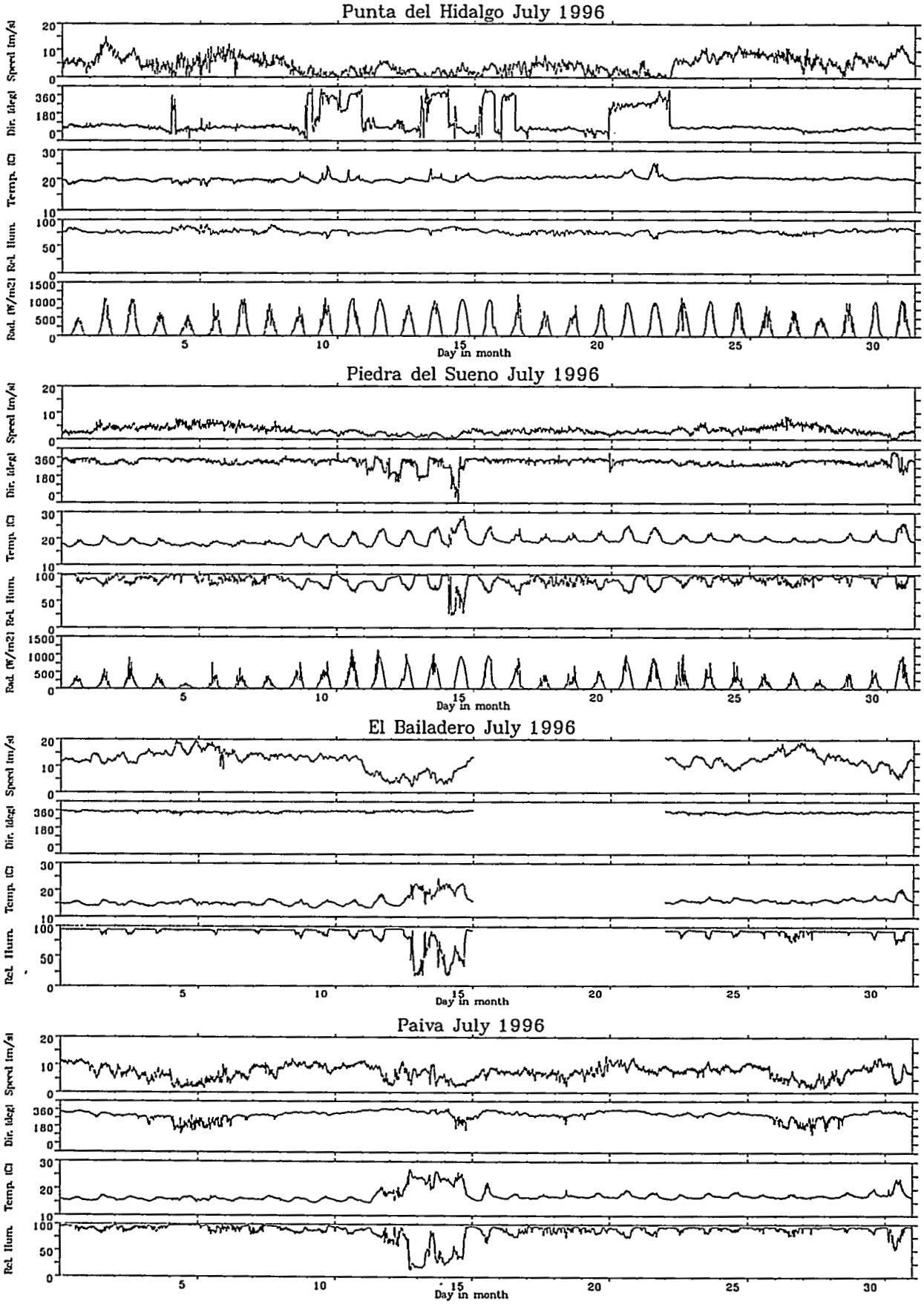

Figure 15. Time series of meteorological measurements in July 1997. The ACE-2 pre-campaign stoped on 12 July.

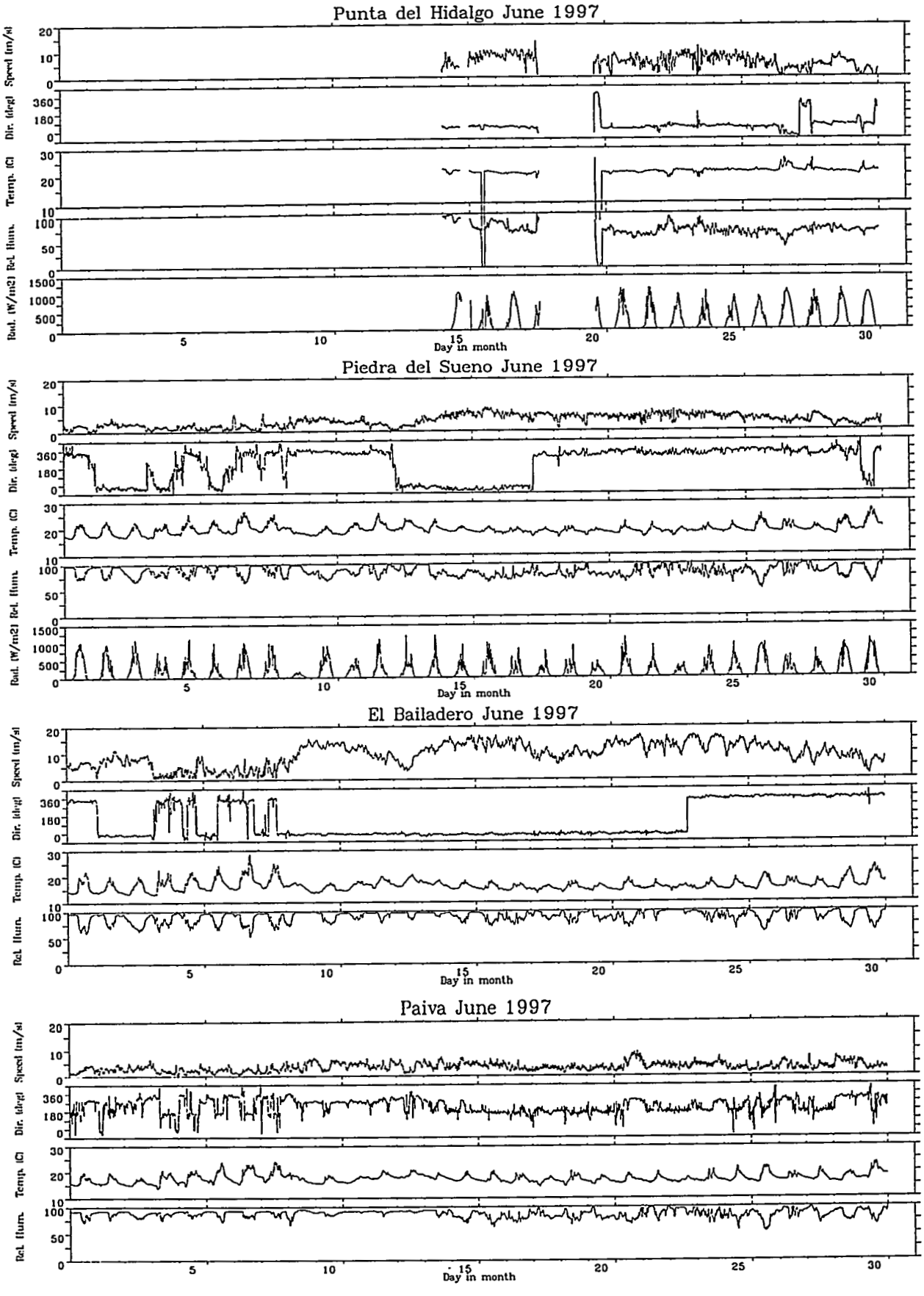

Figure 16. Time series of meteorological measurements in June 1997. The main ACE-2 campaign started on 16 June.

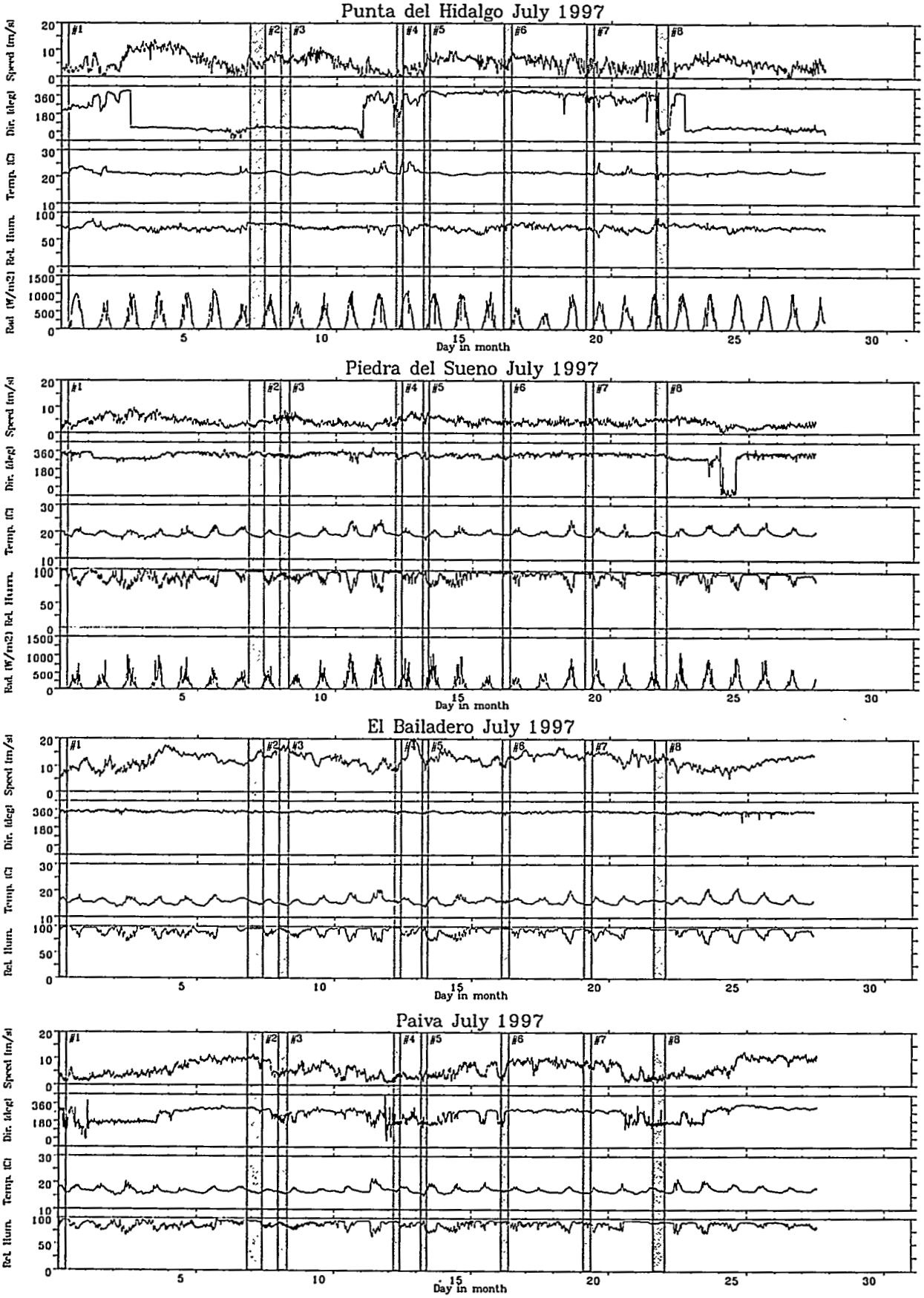

Figure 17. Time series of meteorological measurements in July 1997 with indication of the Hillcloud intensive runs.

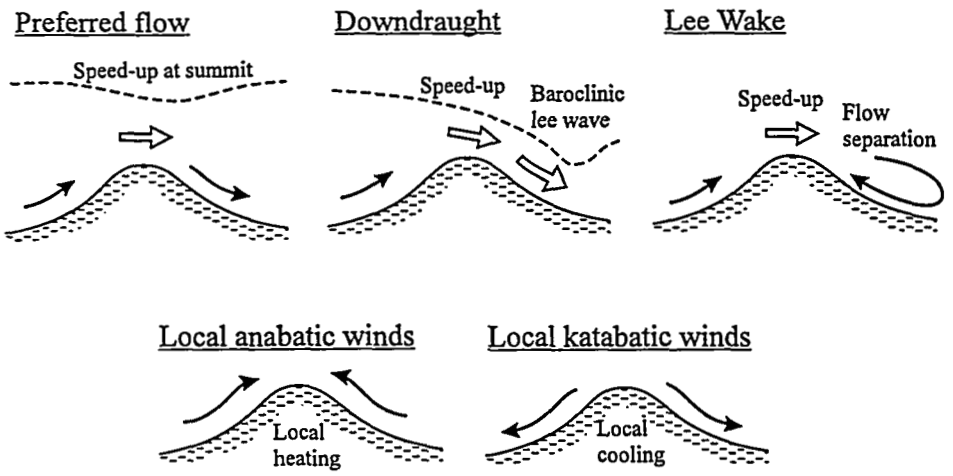

	Upslope	Summit	Downslope	Measuring conditions
Preferred	$\longrightarrow$	$\Longrightarrow$	$\longrightarrow$	Optimal
Downdraught	$\rightarrow$	$\Rightarrow$	$\Rightarrow$	Possible entrainment
Wake	$\longrightarrow$	$\Longrightarrow$	$\longleftarrow$	Unpredictable recycling
Anabatic	$\rightarrow$	$(\rightleftarrows)$	$\longleftarrow$	Decoupled flows
Katabatic	$\longleftarrow$	$(\rightleftarrows)$	$\rightarrow$	Decoupled flows

Figure 18. Flow pattern definitions and corresponding winds at measuring stations.

3.3 Flow classification

The visual examination of detailed time series above leads to speculations about the flow over the Agana peninsula. Figure 18 is a definition sketch of three characteristic flow types driven by synoptic wind and two types of local winds driven by thermal forcing. The flows driven by synoptic winds may be mirrored.

Preferred flow: The flow orientation was often the same at all three sites with minor modifications caused by the channeling effect of the Taganana and San Andres valleys and acceleration at the summit. This situation is prefersble in the context of the HILLCLOUD aerosol experiment.

Downdraught: It is plausible that terrain-induced vertical movements sometimes were in baroclinic resonance with the stratified lower atmosphere and that associated leeward downdraughts occasionally caused strong ground-level leeward winds. Judged from the measured time series, this mainly happend in situations with moderate wind speed at the summit. The downdraughts might generate additional turbulence which could entrain air from above and disturb the aerosol experiment. The significance of possible entrainment depends on the vertical distance to the entrainment zone, and whether the vertical difference of a given concentration was comparable to differences resulting from aerosol processing.

Wake: Sometimes the flow reversed at the rear side of the mountain even though the upstream wind was steady. The most likely reason is flow separation from the sharp mountain ridge. The reverse flow was usually weak and sometimes it alternated with the preferred flow situation. On these conditions leeward aerosol measurements could be contaminated by local pollution and recycled air. The problem did not affect upslope and summit measurements.

Anabatic: Local upslope winds developed in case of weak synoptic wind and heating by solar radiation. Flows in the Taganana and San Andres valleys were disconnected and the wind at the summit could be in either direction or vanish. Anabatic flows were of no practical significance in the present context since the associated temperature rise and humidity drop inhibited capping cloud formation.

Katabatic: Similar local downslope winds developed in case of weak synoptic wind and radiative cooling. Katabatic winds mainly occurred at night and usually during periods with daytime anabatic winds.

Classification scheme

The measured time series were interpreted in terms of these flow types. For convenience, this was done by a computer program using the following simplified classification scheme:

- With the same flow orientation at all sites and
  1. lee wind speed *less* than 75% of the wind at the summit: Preferred
  2. lee wind speed *more* than 75% of the wind at the summit: Downdraught
- With *downslope* winds at both sides of the mountains: ..... Katabatic
- With *upslope* winds at both sides of the mountain and
  1. summit wind speed *weaker* than the average of slope winds: Anabatic
  2. summit wind speed *stronger* than the average of slope winds: Wake
- With same orientation on the slopes but reversed flow at the summit: ... ?

Although these discrimination rules seem rather crude, the results are in good accordance with subjective judgments by visual examination of the time series. Table 2 shows a frequency distribution of winds based on the classification scheme and periods with wind data available[5] from all stations. It is seen that

1. the preferred flow situation occurred in 37% of the time,
2. downdraught situations with possible entrainments occurred in 11% of the time,
3. unfavourable wake flows were just as frequent (37%) as the preferred flow,
4. unfavourable local winds were relatively rare (14%) and mainly katabatic wind systems in winter nights,
5. winds from northerly directions were much more frequent (79%) than southerly winds (6%).

The flow types experienced under the 1996 pre-campaign and the main ACE-2 campaign are perhaps of greater practical interest than yearly statistics. These are indicated in tables 3 and 4.

4 Radiosonde measurements

The atmospheric boundary layer in the ACE-2 area is usually capped by inversion at an altitude comparable to or twice the height of the Anaga mountain range. The altitude and strength of this inversion affect the surface winds, eg a strong inversion at low altitude probably enhances the wind speed-up in the passage

[5]Missing wind direction data from Piedra del Sueno ruled out the autumn data.

Table 2. Frequency distribution of the flow situations defined in figure 18.

	Preferred		Down		Wake		Local		Unknown
	N	S	N	S	N	S	Anabat	Katabat	
Jun96	68%	–	–	–	32%	–	–	–	–
Jun96	41%	–	36%	–	18%	–	–	5%	–
Aug96	45%	–	16%	–	38%	–	–	–	–
Sep96	38%	5%	4%	–	45%	–	–	8%	–
Jan97	15%	15%	–	3%	40%	–	1%	23%	3%
Feb97	10%	14%	7%	3%	29%	–	2%	31%	4%
Mar97	33%	10%	8%	3%	28%	–	–	17%	–
Apr97	35%	3%	11%	2%	32%	–	3%	13%	1%
May97	29%	–	7%	–	51%	–	3%	9%	1%
Jun97	32%	–	2%	–	55%	–	3%	6%	1%
Jul97	47%	–	12%	–	40%	–	–	–	–
Total	32%	5%	10%	1%	37%	–	2%	12%	1%

Table 3. Flow types during part of the 1996 pre-campaign: ▪ preferred flow, ▯ possible downdraught, ▮ wake, and local katabatic winds ↓. With exception of the latter, the flow orientation was toward south.

Date	Time 0 6 12 18 24	Comments
June 24		Missing El Bailadero data
June 25		
June 26		
June 27		
June 28		180
June 29		
June 30		
July 1		Downdraught
July 2		
July 3		Favourable conditions 185
July 4		
July 5		Wake flow
July 6		
July 7		
July 8		Favourable conditions 190
July 9		Occasional downdraught
July 10		
July 11		
July 12		Nocturnal katabatic flows

at El Bailadero. A leeward downdraught is expected when the time scale of a baraoclinic gravity wave matches the passage time. Information on the upper air flow and stratification was therefore necessary for accurate flow modelling and humidity profiles were needed in order to understand hill cap cloud formation.

As part of the general weather survey Institudo National Meteorología (INM) launches radiosondes from Santa Cruz on a routine basis. It was however felt that the lowest part of these profiles might not be representative for the flow on

Table 4. Flow types during ACE-2 1997 and timing of Hillcloud intensive runs: - preferred flow, [] possible Paiva downdraught, ▮ wake at Paiva, ↑ local anabatic winds, and local katabatic winds ↓. With exception of local anabatic and katabatic winds, the flow orientation was toward south. Comments to overnight runs are listed under the following day.

Date	Time 0 6 12 18 24	Comments
June 16		
June 17		
June 18		
June 19		170
June 20		
June 21		
June 22		
June 23		
June 24		175
June 25		
June 26		
June 27		
June 28		
June 29		180
June 30		
July 1		RUN1: 23:40–6:30 (Paiva wake at dawn)
July 2		
July 3		
July 4		185
July 5		
July 6		
July 7		
July 8		RUN2: 20:00–9:30 (initial downdraught)
July 9		RUN3: 23:00–7:30 (Paiva wake) 190
July 10		
July 11		
July 12		
July 13		RUN4: 4:00–?? (Paiva wake)
July 14		RUN5: 4:00–9:30 (Paiva wake) 195
July 15		
July 16		
July 17		RUN6: 2:00–9:30 (night wake)
July 18		
July 19		200
July 20		RUN7: 2:00–9:30 (favourable flow)
July 21		
July 22		RUN8: 14:30–1:00 (Paiva wake)
July 23		
July 24		205
July 25		
July 26		

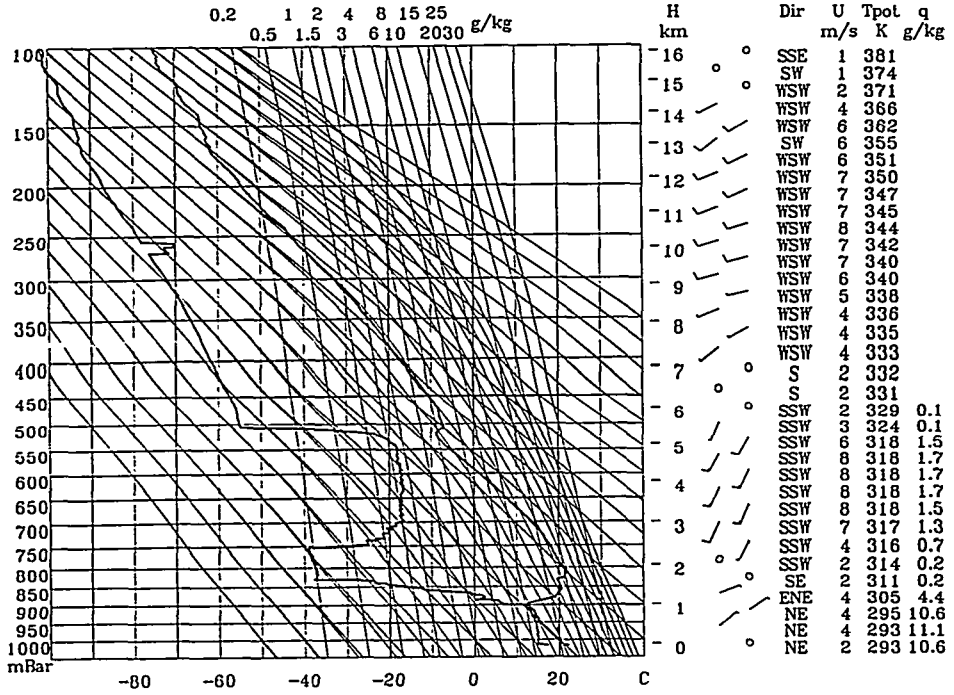

Figure 19. Punta de Hidalgo, June 8 1997, 06 UTC (Run 2): Pseudo-adiabatical diagram with wind symbols and key parameters.

the northern coast of Tenerife and it was decided to launch an additional series of Vaisala RS80 radiosondes from Punta del Hidalgo during the main ACE-2 campaing. This field work was done by the JRC.

The RS80 sonde transmits measurements of temperature, humidity and pressure to a ground-based reciving station which also tracks the flight path. Initial data processing by the recieving station provides the following parameters: *data provided*

- flight time [s],
- height h [m],
- pressure p [hPa],
- temperature t [°C],
- relative humidity RH [%],
- dew-point temperature t_{dew} [°C],
- wind direction Dir [°],
- wind speed U [m/s]

In the ACE-2 campaign these signals were recorded with enhanced time resolution, ie every 2 s for the first 20 min of the flight and every 10 s thereafter. Presumably the recieving station derived the dew-point temerature t_{dew} from the relative humidity and temperature signals and calculated the height as an integral based on pressure, temperature and humidity signals. The wind direction was measured clockwise from north as usual.

Figure 19 shows an example of temperature and dew-point temperature profiles (thick solid lines) plotted in a pseudo-adibatical diagram. From the thin auxiliary lines it may be seen that the potential temperature and water content were fairly constant in the boundary-layer part of the profile. The cloud base appears as the level where the two temperature signals approached each other ($\approx$ 600 m), the *example*

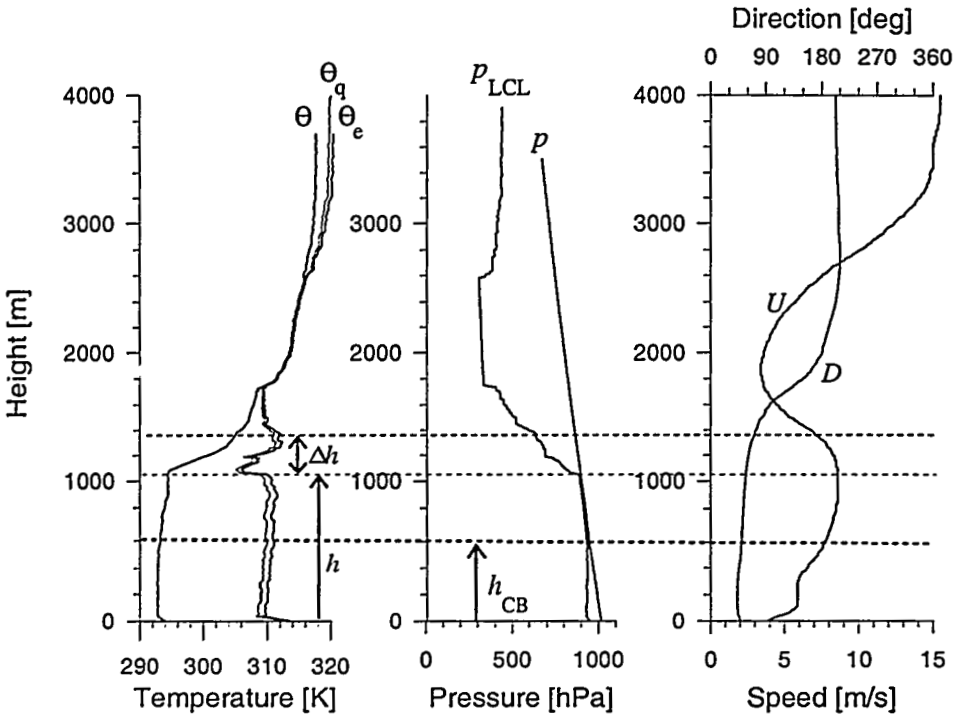

Figure 20. Punta de Hidalgo, June 8 1997, 6:00 (Run 2): Radiosonde profiles of potential temperature θ, wet equivalent potential temperature θ_q, equivalent potential temperature θ_q, pressure p, lifting condensation pressure p_{lcl}, wind speed u and wind direction Dir. Dashed lines indicate inversion height and top of the capping layer.

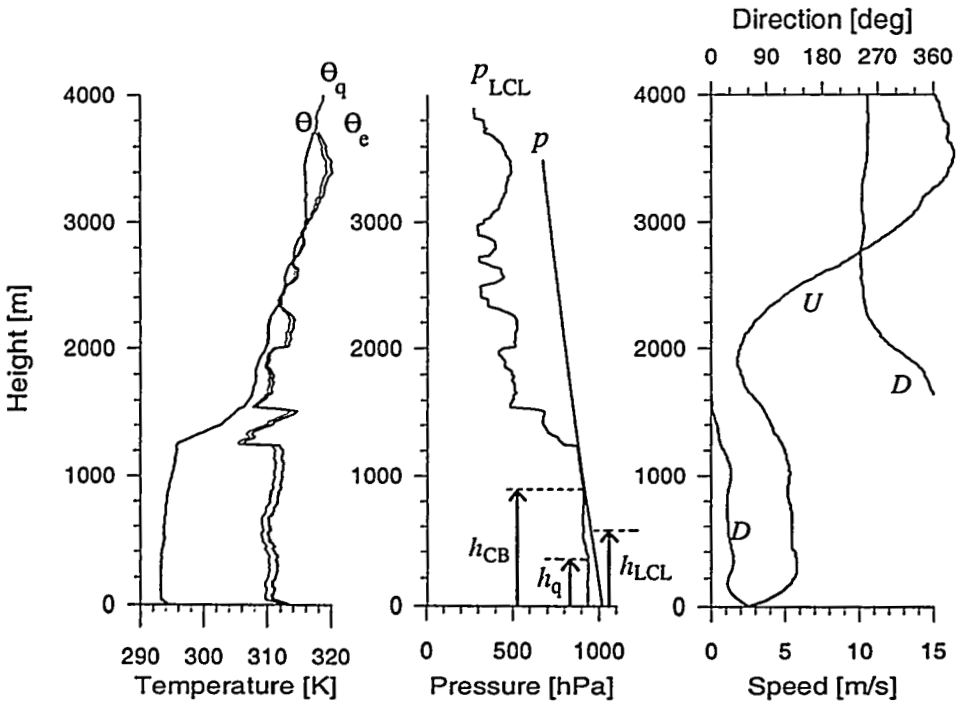

Figure 21. Punta de Hidalgo, June 17 1997, 0:00 (Run 6): Radiosonde profiles as in figure 20. Dashed lines indicate inversion height, top of the capping layer and level of condensation.

inversion height is the onset of the sharp temperature gradient ($\approx$ 1000 m) and the top of the capping layer ($\approx$ 1500 m) is the upper limit of the strong thermal stratification. The water content was $\approx$ 10 g/kg in the boundary layer, close to zero above the capping layer and $\approx$ 2 g/kg in a relatively moist layer from 3 to 6 km. The wind speed was modest at all heights and the wind direction veered clockwise from NE in the boundary layer to WSW at high altitudes.

Analysis

Features of main interest are the depth and uniformity of the boundary layer, the height and strength of the inversion, the above stratification, and the level of the cloud base. Sometimes the water vapour was imperfectly mixed within the boundary layer and near-surface humid air could condense by adiabatic expansion during passage of the mountain.

data derived

The following diagnostic data are derived from the parameters provided by the recieving station, see appendix A.

- potential temperature θ [K],
- equivalent potential temperature θ_e [K],
- wet equivalent potential temperature θ_q [K],
- water vapour mixing ratio q $[g/kg]$,
- pressure of lifting condensation level p_{LCL} [hPa],
- Brunt-Vaisala frequency squared N^2 [s^{-2}]

The potential temperature θ is conserved during adiabatic expansion of dry air and profiles of potential temperature give a good description of atmospheric stability. The equivalent potential temperature θ_e is a slightly different parameter which includes the latent heat of the water content. It is conserved in the socalled 'pseudo-adiabatical' process in which condensed water is separated from the air mass leaving only the heat of condensation. The wet equivalent potential temperature θ_q is an alternative parameter based on the opposite assumption that all of the liquid water follows the air mass as an aerosol fraction. The water vapour mixing ratio q is an alternative description of the humidity and pressure of the lifting condensation level p_{lcl} is the condition where the moisture of an adiabatically expanded air parcel starts to condensate. The Brunt-Vaisala frequency is defined by $N^2 = g/\theta \cdot d\theta/dz$. This is the natural frequency of baroclinic gravity waves in a continuously stratified fluid.

Figures 20 and 20 show vertical profiles of selected parameters. The inversion height h and depth of the capping layer are detected by the potential temperature θ profile in the leftmost frame. These heights are indicated by the upper two horizontal dashed lines in figure 20. The third dashed line indicates the cloud base h_{cb}, ie the height where the lifting condensation pressure p_{lcl} approaches the atmospheric pressure p. In figure 20 this is above the height of the Anaga mountain range ($\approx$ 700 m). Near-surface air may however condensate by elevation to the liquid condensation level h_{lcl}. Table 5 is a compilation of these deduced parameters. The two-kink parametrisation of the potential temperature profile, shown in the upper vignette beside the table, was obtained by linear regression of three subjectively prescribed data subranges. The determination of cloud base and height of condensation was entirely subjective and probably less accurate than the two-kink parametrization. One problem was that often the pressure curves did not touch completely, ie the relative humidity signal reached a maximum slightly less than 100%. The apparent undersaturation was judged to be a calibration problem

Table 5. Two-kink parametrisation of radiosonde profiles and estimates of cloud base and lifting condensation levels.

Time	h [m]	Δh [m]	θ [K]	$\frac{\Delta\theta}{\Delta h}$ [K/m]	Γ [K/m]	h_{CB} [m]	h_{LCL} [m]	Δh_q [m]	
19/6:12	1764	800	292.6	0.025	0.0032	1140	?	?	Reduced resolution
25/6:00	1505	171	293.4	0.063	0.0058	?	?	?	Reduced resolution
26/6:12	1531	94	293.8	0.130	0.0044	1500	?	?	Reduced resolution
4/7:00	1629	433	292.7	0.031	0.0048	?	1100	600	Reduced resolution
5/7:12	1638	177	292.5	0.077	0.0043	?	?	?	Reduced resolution
7/7:00	1155	135	292.7	0.062	0.0098	900	–	–	
7/7:12	1243	250	292.8	0.058	0.0062	730	–	–	
8/7:00	936	209	293.6	0.045	0.0112	930	650	120	
8/7:06	1025	364	293.4	0.039	0.0072	600	–	–	Run 2: 20:00-9:30
9/7:00	807	249	293.2	0.045	0.0082	790	700	150	Run 3: 23:00-7:30
9/7:06	956	211	292.7	0.050	0.0150	900	–	–	
9/7:12	995	141	292.6	0.075	0.0141	900	–	–	
11/7:12	873	127	292.7	0.065	0.0061	850	–	–	
12/7:00	1115	641	293.5	0.021	0.0050	700	–	–	
13/7:00	1415	232	293.8	0.048	0.0053	1300	700	400	Run 4: 1:00-8:00
14/7:00	1753	239	294.5	0.041	0.0065	650	–	–	Run 5: 4:00-9:30
14/7:12	811	–	292.9	–	0.0079	800	–	–	No capping layer
15/7:00	1680	274	293.4	0.041	0.0064	850	–	–	
15/7:12	1502	176	293.4	0.063	0.0060	920	–	–	
16/7:00	1328	311	293.0	0.044	0.0053	–	1100	400	
16/7:12	1251	109	293.2	0.116	0.0044	1250	1080	350	
17/7:00	1171	432	294.0	0.034	0.0039	900	650	370	Run 6: 2:00-9:30
17/7:12	1118	265	293.6	0.055	0.0033	550	–	–	
18/7:12	1075	343	293.8	0.045	0.0033	870	–	–	
19/7:00	1200	140	293.2	0.104	0.0037	900	850	50	
19/7:12	1236	126	294.2	0.099	0.0042	1200	950	200	
20/7:00	1140	209	293.2	0.066	0.0039	800	–	–	Run 7: 2:00-9:30
20/7:12	1283	362	292.7	0.041	0.0040	1200	1000	700	
21/7:00	1206	429	293.5	0.029	0.0047	850	–	–	
21/7:12	1111	359	293.2	0.033	0.0047	1100	950	300	
22/7:00	1265	133	293.8	0.073	0.0055	1200	–	–	Reduced resolution
22/7:12	1191	517	293.6	0.022	0.0047	1050	750	500	Run 8: 14:30-24:00
23/7:00	1186	1031	293.4	0.015	0.0047	–	840	530	
23/7:12	1468	279	294.2	0.031	0.0080	–	870	600	
24/7:12	1438	485	294.1	0.026	0.0047	–	850	500	

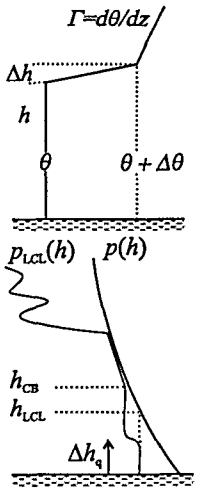

in case the signal reached a steady maximum. Another problem was that the lower undersaturated part of the lifting condensation profiles p_{lcl} was often less regular than sketched in the second vignette of table 5 and this compromised the h_{lcl} and Δh_q parametrisation.

overview

Figure 4 provides an overview of the radiosonde profiles and the estimates from table 5. Each wind profile is indicated by a column of arrows of variable thickness and orientation indicating speed and flow direction, eg a thick downward arrow means strong flow toward S and a thin left arrow means weak flow toward E. The thick broken lines indicate inversion height h and top of the capping layer $h + \Delta h$. The inversion height varied from just above the summit to about twice this level. The thin broken line below the inversion height indicates the cloud base h_{cb}. On some occasions this almost approached the summit level. The boxes with

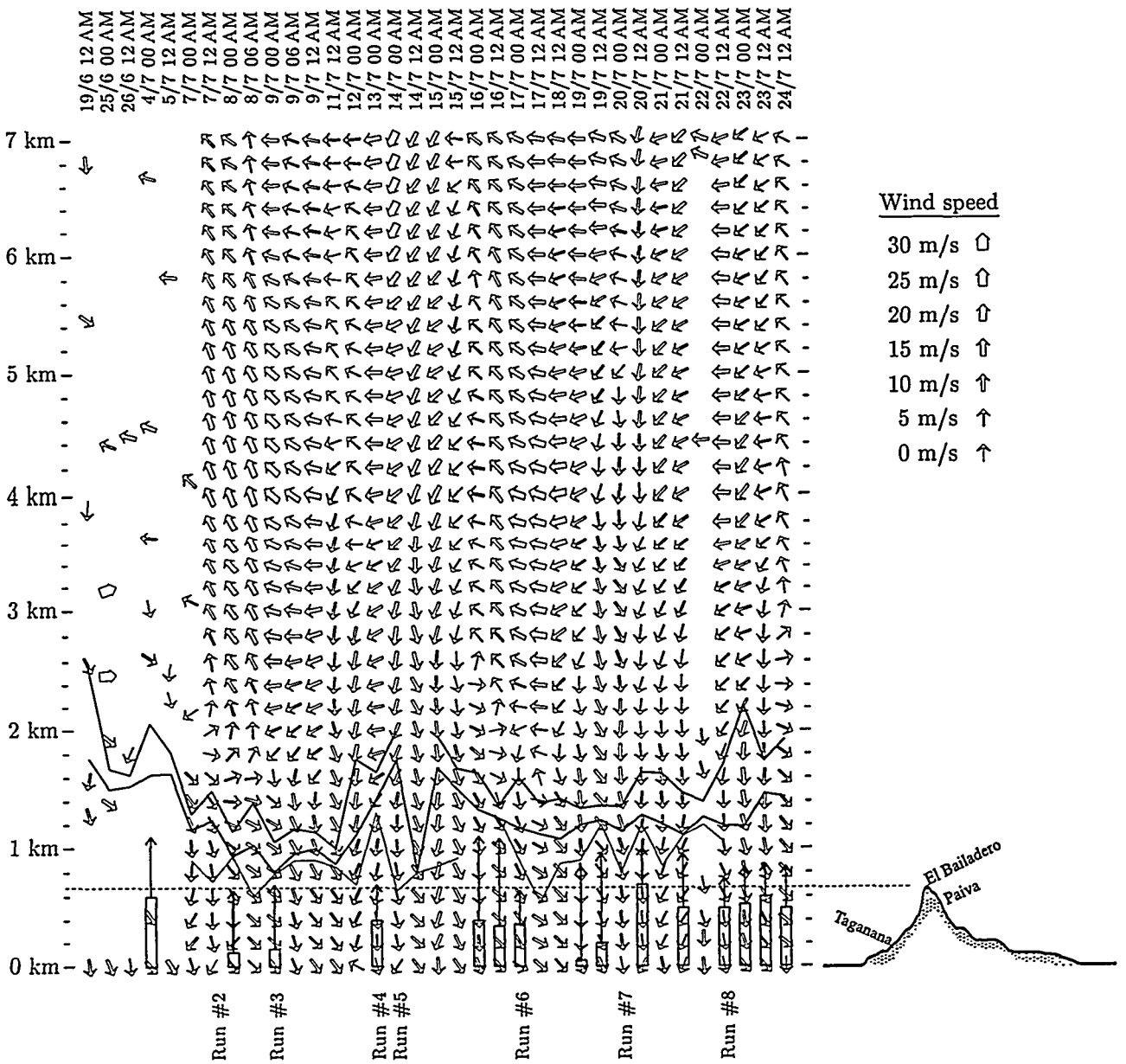

Figure 22. Overview of radiosonde profiles. Arrows of variable thickness indicate wind speed and direction as a function of height. The broken lines indicate estimates of cloud base h_{CB}, inversion height h and top of capping layer $h + \Delta h$. The slender vertical arrows indicate estimated lifting condensation levels h_{LCL}, see table 5.

the slender veritical arrows above indicate the thickness of a moist surface layer h_q and the level h_{lcl} where it starts to condense. The condition for hill cap formation is either a cloud base or lifting condensation level below the summit level. The two situations are slightly different: a low cloud base means that all of the boundary layer was sufficiently moist for condensation during passage of the ridge, whereas a low condensation level indicates that only a thin layer may condense. Ideally these conditions should coincide with the HILLCLOUD run times, ie when liquid cloud water was actually observed at the summit. They generally do but with some discrepancies which reflect uncertainties in the profile analysis or differences in timing.

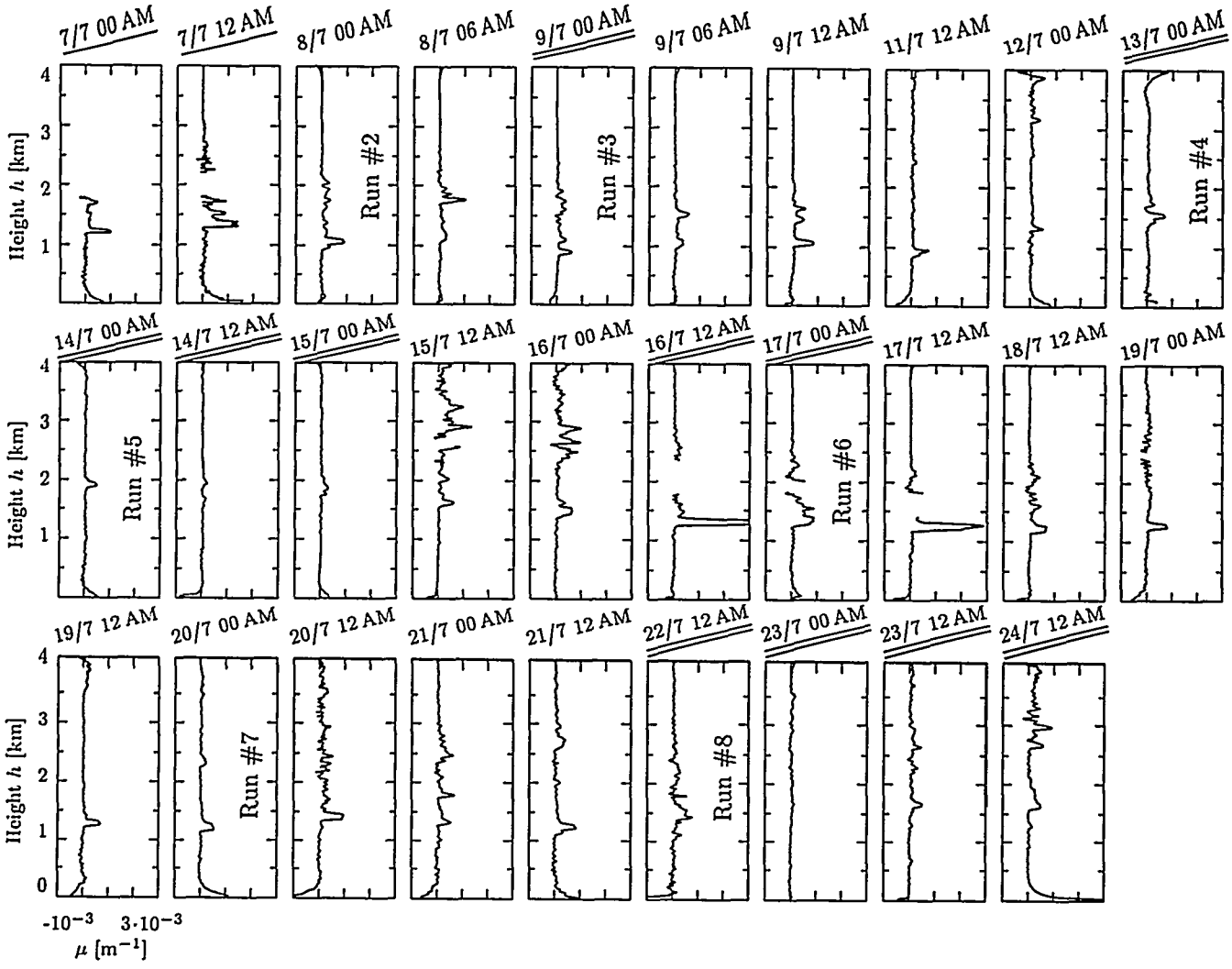

Figure 23. The stability parameter $\mu = N/u$ (with the Brunt-Vaisala frequency defined by $N^2 = g/\theta \cdot d\theta/dz$) as a function of height. The launching time above each plot is underlined by a single or double line in case the surface observations suggest strong downflow or wake re-circulation, see table 4.

flow stability

The atmospheric stability influences the airflow. Carruthers & Choularton (1982) presents a two-dimensional model of flow over hills, see Appendix B. The model input is the terrain topography and stability parameter $\mu = N/u_0$ defined by the Brunt-Vaisala frequency N and the unperturbed advection u_0 which is assumed to be approximately constant. Figure 23 shows vertical profiles of this stability parameter. Data with wind direction more than 60° off the N direction or with wind speed less than 2 m/s are excluded from the plots. The flow classes found by the ground-based observations are indicated by one or two lines under the launching times. The connection between flow classes and stability profiles is not transparent, although wake flow usually occurred in case of weak stratification.

cloud observations

The top frame in figure 24 shows a time series of 30-min average measurements of the cloud base by a ceilometer at the Hillcloud upslope site. Intermittent clear-sky measurements are excluded from the average values. The difference between the altitudes of the summit site and the Hillcloud upslope site in Taganana is indicated by the dashed line. Sometimes the cloud base is seen to approach this level. The lower frame shows liquid water content measured at El Bailadero and shaded areas indicate the timing of the Hillcloud intensive runs. Cloud base levels measured to be comparable to the height of the mountain range do not always

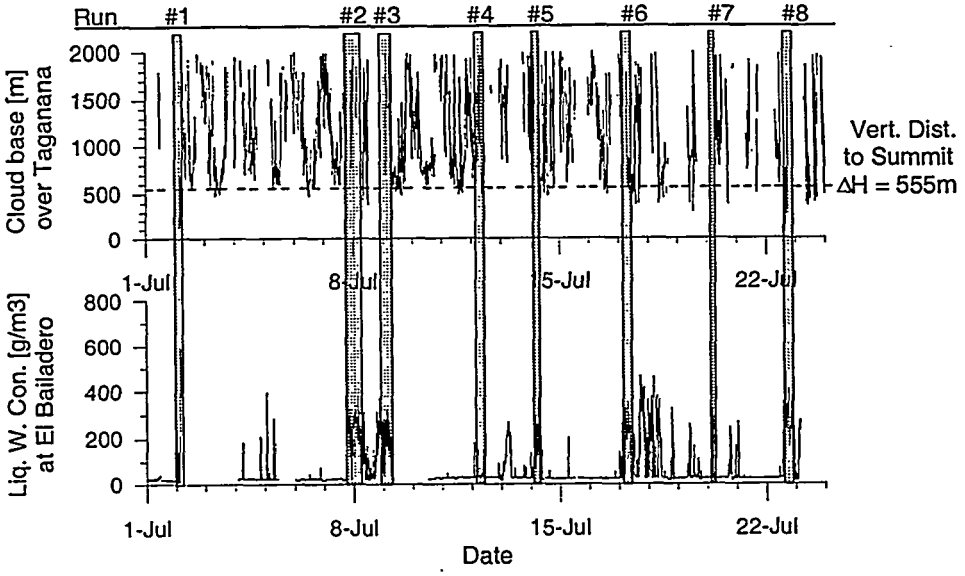

Figure 24. Cloud base over Taganana deduced from ceilometer measurements and liquid water content measured at El Bailadero.

coincide with cloud presence at the summit, eg run 3. Thus the upstream extent of the hill cap cloud was often shorter than the horizontal distance between these measuring stations or less than 600 m.

5 Conclusions

Meteorological stations were installed at the summit of the Anaga mountain ridge and in two valleys on the northern and southern slopes. They were operated for more than one year in a period covering both the 1996 pre-campaign and the main ACE-2 campaign. Initial technical difficulties were solved and no errors were experienced during the main campaign. Ten-minute average data of wind speed, wind direction, temperature and relative humidity are available from all stations. An additional solar radiation signal is available from the northern slope.

A digital terrain model was obtained by digitisation of height contours from a 1:25.000 map of the Taganana valley, spliced with a similar but coarser digitalisation of the whole island produced by the Universite Blaise Pascal. Interpolated terrain heights in orthogonal grids suitable for numerical computations are available on request.

Data from the meteorological stations in the Taganana area plus a similar coastal station operated by JRC were compared to each other. Previous mesoscale flow simulations (Troude 1996) had shown that the prevailing trade winds were blocked by the tall island and forced almost perpendicularly over the Anaga peninsula. The field observations confirm this general flow pattern and suggested some additional local effects:

- Valley flows were canalised along the valley axes and local speed and direction were often quite different from the coastal winds. Rare local flows not following the valley axes were moderated by terrain shelter;

- The summit flow was accelerated and forced in directions perpendicular to the mountain ridge. The reason was probably a strong pressure difference;

- Generally the flow was from north to south. This happened in 79% of the time and the exceptions were mainly in winter;
- Sometimes the flow reversed on the leeward side and on some occasions this situation alternated with the normal flow. The reverse-flow wind speed was relatively weak and the phenomenon was probably caused by flow separation from the mountain ridge. This happened in 37% of the time;
- In spite of the situations with relatively calm wake circulation the average wind speed was strongest on the leeward side of the mountain, regardless of the general flow orientation. This statistical bias is interpreted as a sign of baroclinic downdraughts;
- Local valley winds forced by radiative cooling or heating were observed in situations with weak synoptic wind. This happened in 14% of the time and mainly in the winter months;
- The temperature was more stable at Punta del Hidalgo than at the inland sites. This indicates some heat transfer from the ground;
- The average solar radiation was weaker in the Taganana valley than at the coast. This is a sign of local hill cap clouds;
- The relative humidity was generally high and often reached saturation at night. Southerly winds in winter were sometimes exceptionally dry;

During the main campaign the JRC launched a series of radiosondes from the northern coast. A table of inversion height, height and strength of the capping layer and the above stratification was deduced from potential temperature profiles. The potential temperature profiles were 'classic' with a well-mixed boundary layer, a strongly stratified inversion zone and weaker stratification above. Wind speed and direction were quite dependent on height. Humidity profiles were used to calculate the cloud base and level of condensation of moist near-surface air. The radiosonde analysis of possibilities for hill cap cloud formation is in reasonable agreement with the actual cloud observations by UMIST.

Acknowledgement

Jose Luis Megia and Carmen Jimenez from Institudo National Meteorología (INM) provided invaluable local contacts. The Risø meteorological stations were installed and serviced by Jan Nielsen and Søren Lund. Helena Gonzales (University of La Laguna) collected our data storage units and Gunner Jensen (Risø) made quality control and data debugging. The supplementary meteorological time series from the Punta del Hidalgo light house were measured by Frank McGovern (JRC). The radiosondes were purchased by UMIST, launced by Rita van Dingenen and Aki Olavi Virkkula (JRC) and the radiosonde signals were recieved by equipment borrowed from INM. The low-resolution terrain digitalisation was provided by Universite Blaise Pascal and the high-resolution local area digitalisation was made by Rasmus Paulsen (Risø). The cloud base observations at Taganana and liquid water content measurements at El Bailadero were performed by UMIST.

References

Carruthers, D. J. & Choularton, T. W. (1982). Airflow over hills of moderate slope, *Quart. J. R. Meteorol. Soc.*, **108**, 603–624.

Chandler, A. S., Choularton, T. W., Dollard, G. J., Gay, M. J., Hill, T. A., Jones, A., Morse, A. P., Penkett, S. A. & Tyler, B. J. (1988). A field study of the cloud chemistry and cloud microphysics at Great Dunn Fell, *Atmos. Environ.*, **22**, 683–694.

Choularton, T. W., Wicks, A. J., Downer, R. M., Gallagher, M. W., Penkett, S. A., Bandy, B. J., Dollard, G. J., Jones, B. M. R., Davies, T. D., Gay, M. J. & Tyler, B. J. (1992). A field study of the generation of nitrate in a hill cap cloud, *Environ. Pollut.*, **75**, 69–73.

Gallagher, M. W., Downer, R. M., Choularton, T. W., Gay, M. J., Stromberg, I., Mill, C. S., Radojevic, M., Tyler, B. J., Bandy, B. J., Penkett, S. A., Davies, T. D., Dollard, G. J. & Jones, B. M. R. (1990). Case studies of the oxidation of sulphur dioxide in a hill cap cloud using ground and aircraft based measurements, *J. Geophys. Res.*, **95**, 18.517–18.537.

Paluch, I. R. (1979). The entrainment mechanism in Colorado cumuli, *J. Atmos. Sci.*

Troude, F. (1996). *Simulation tridimensionelle d'écoulement orographiques autour ténériffe*, Master's thesis, Universite Blaise Pascal, Clemont Ferrand. (In French).

A Parameters for radiosonde analysis

The total entropy of a mixture of dry air, water vapour and liquid water is the sum of specific entropies of three components

$$s = s_{\mathrm{a}} + q s_{\mathrm{v}} + l s_{\mathrm{w}} \tag{A.1}$$

where q and l are mixing ratios for vapour and liquid water defined as masses of vapour and liquid water content divided by mass of dry air. With the ideal gas assumption the specific entropies are given by

$$s_{\mathrm{a}} = c_p^a \ln T - \frac{R}{M_a} \ln p \tag{A.2}$$

$$s_{\mathrm{v}} = c_p^v \ln T - \frac{R}{M_w} \ln e \tag{A.3}$$

$$s_{\mathrm{w}} = c_p^w \ln T \tag{A.4}$$

where M_a, M_w are the molar weights, c_p^a, c_p^v and c_p^w are heat capacities for dry air, water vapour and liquid water respectively, p is pressure, e is partial pressure of water vapour and R is the universal gas constant. The entropy difference between the two water phases is related to the temperature dependent by latent heat $L(T)$.

$$s_{\mathrm{v}} - s_{\mathrm{w}} = \frac{L(T)}{T} \tag{A.5}$$

The latent heat variation may be approximated by

$$\frac{dL}{dT} = c_p^v - c_p^w \Rightarrow L(T) \simeq L_0 + \Delta c_p (T - T_{\mathrm{o}}) \tag{A.6}$$

where L_0 is the latent heat at a reference temperature T_0 and the heat capacity difference $\Delta c_p = c_p^v - c_p^w$ is negative. At equilibrium saturation pressure there is no driving potential for further phase transition, and Gibbs' free energy of the two phases is equal. This must be the case for any state of condensation $e_{\mathrm{sat}}(T_{\mathrm{sat}})$ and increments of Gibbs' free energy must be equal in the two phases

$$dg_v = dg_w \qquad \text{(at saturation vapour pressure)} \tag{A.7}$$

These change of Gibbs' free energy may also be written $dg = -sdT + \alpha de_{\mathrm{sat}}$ (with α as the specific volume) and the saturation pressure curve is described by

$$\frac{de_{\mathrm{sat}}}{dT} = \frac{s_v - s_w}{\alpha_v - \alpha_w} = \frac{L}{T(\alpha_v - \alpha_w)} \simeq \frac{Le_{\mathrm{sat}}}{RT^2} \tag{A.8}$$

The approximation is based on assumptions of ideal gas and negligible specific liquid phase volume $\alpha_v \gg \alpha_w$. By use of the latent heat approximation in equation A.6 the temperature variation is integrated to

$$\frac{e_{\mathrm{sat}}}{e_{\mathrm{sat}}(T_0)} \simeq \exp\left\{\frac{L_0 - \Delta c_p T_0}{R}\left(\frac{1}{T_0} - \frac{1}{T}\right) + \frac{\Delta c_p}{R}\ln\left(\frac{T}{T_0}\right)\right\} \tag{A.9}$$

The actual water vapour pressure in the atmosphere e is related to the relative humidity RH defined by

$$RH = \frac{e}{e_{\mathrm{sat}}(T)} \cdot 100\ \% \tag{A.10}$$

and the dew point temperature T_{dew} is the temperature of condensation

$$e = e_{\mathrm{sat}}(T_{\mathrm{dew}}) \tag{A.11}$$

potential temperature θ

The potential temperature θ is defined as the temperature obtained by adiabatic compression to a reference pressure p_0 (1000 hPa). The specific air entropy s_{a} is conserved during this process implying that

$$c_p^a \ln T - \frac{R}{M_a}\ln p = \text{constant} \Rightarrow \theta = T\left(\frac{p_0}{p}\right)^{\frac{R}{M_a c_p^a}} \approx T\left(\frac{p_0}{p}\right)^{0.286} \tag{A.12}$$

equivalent potential temperature θ_e

Expansion of humid air eventually leads to condensation. The so-called 'pseudo-adiabatic' expansion is a process where water droplets are assumed to rain out of the air leaving only the latent heat. The equivalent potential temperature θ_e is defined as the temperature obtained by initial adiabatic expansion to the condensation level (if undersaturated), followed by pseudo-adiabatic compression until all moisture is removed and by adiabatic compression to the reference pressure p_0. The entropy contribution Δs from water condensation increases the equivalent potential temperature θ_e relative to the ordinary potential temperature:

$$s_{\mathrm{a}} + \Delta s = c_p^a \ln T - \frac{R}{M_a}\ln p + \frac{qL}{T} \Rightarrow \theta_e = \theta \cdot \exp\left\{\frac{qL}{c_p^a T}\right\} \tag{A.13}$$

wet equivalent potential temperature θ_q

In the absense of precipitation it may be more relevant to consider a wet adiabatic process where a liquid aerosol fraction remains in the air parcel. Paluch (1979) explains that the total entropy during wet adiabatic expansion of a saturated air parcel is

$$\begin{aligned} s &= s_{\mathrm{a}} + qs_{\mathrm{v}} + ls_{\mathrm{w}} = s_{\mathrm{a}} + \frac{qL}{T} + (q+l)s_{\mathrm{w}} = \text{constant} \Rightarrow \\ &(c_p^a + Qc_p^w)\ln T - \frac{R}{M_a}\ln p + \frac{qL}{T} = \text{constant} \end{aligned} \tag{A.14}$$

Here we define the total water content $Q = q + l$ and make use of equation A.5. The wet equivalent potential temperature θ_q under *saturated* conditions is then defined as the temperature obtained by integration to the reference pressure p_0.

$$\begin{aligned}\theta_q^{\text{sat}} &= T\left(\frac{p_0}{p}\right)^{\frac{R}{M_a c_p^a}\frac{1}{1+Qc_p^w/c_p^a}} \cdot \exp\left\{\frac{qL}{c_p^a T(1+Qc_p^w/c_p^a}\right\} \\ &\approx T\left(\frac{p_0}{p}\right)^{\frac{0.286}{1+4.19Q}} \cdot \exp\left\{\frac{qL}{c_p^a T}\frac{1}{1+4.19Q}\right\} \end{aligned} \tag{A.15}$$

The entropy budget for adiabatic expansion of *unsaturated* air is slightly different:

$$s = s_a + qs_v = c_p^a \ln T - \frac{R}{M_a}\ln p + q(c_p^v \ln T - \frac{R}{M_w}\ln e) \Rightarrow$$

$$\ln T - \frac{R}{M_a c_p^a}\frac{1+\frac{M_a}{M_w}q}{1+\frac{c_p^a}{c_p^v}q}\ln p = \text{constant} \tag{A.16}$$

The latter equation is obtained by a relation between the partial pressure ratio e/p and the (constant) mixing ratio q which implies that $\ln e = \ln p + \text{constant}$. Integration of this results in the equation

$$\theta_q^{\text{unsat}} = K \cdot T\left(\frac{p_0}{p}\right)^{\frac{R}{M_a c_p^a}\cdot\frac{1+M_a/M_w q}{1+c_p^v/c_p^a q}} \approx K \cdot T\left(\frac{p_0}{p}\right)^{0.286(1-0.26q)} \tag{A.17}$$

where K is an integration constant fixed such that it ensures continuity of the two expressions for θ_q in equations A.15 and A.17 at the liquid condensation level p_{LCL}. The liquid water mixing ratio is zero under the unsaturated conditions, and thus $Q = q$.

$$\begin{aligned} K &= \left(\frac{p_0}{p_{\text{LCL}}}\right)^{\frac{R}{M_a c_p^a}\left(\frac{1}{1+c_p^w/c_p^a q}-\frac{1+M_a/M_w q}{1+c_p^v/c_p^a q}\right)} \cdot \exp\left\{\frac{qL}{c_p^a T(1+qc_p^w/c_p^a)}\right\} \\ &\approx \left(\frac{p_0}{p_{\text{LCL}}}\right)^{-1.13q} \exp\left\{\frac{qL}{c_p^a T}\frac{1}{1+4.19q}\right\} \end{aligned} \tag{A.18}$$

water vapour mixing ratio q

The water vapour mixing ratio q is the water vapour mass divided by the mass of dry air

$$q = \frac{eM_w}{(p-e)M_a} \tag{A.19}$$

lifting condensation level

The lifting condensation level is the pressure where the water content of an adiabatically expanded air parcel starts to condense. The pressure and temperature at the lifting condensation level (p_{lcl}, T_{lcl}) are found by an iterative solution of the equations

$$\frac{e_{\text{sat}}(T_{\text{lcl}})}{p_{\text{lcl}}} = \frac{e}{p} \quad \text{and} \quad \frac{T_{\text{lcl}}}{T} = \left(\frac{p_{\text{lcl}}}{p}\right)^{\frac{R}{M_a c_p^a}} \tag{A.20}$$

Brunt-Vaisala frequency N

The Brunt-Vaisala frequency N is defined by the potential temperature gradient

$$N^2 = \frac{g}{\theta}\frac{\partial\theta}{\partial z} \tag{A.21}$$

The Brunt-Vaisala frequency N in stably stratified layers is the natural frequency of internal waves. Negative values indicate instability.

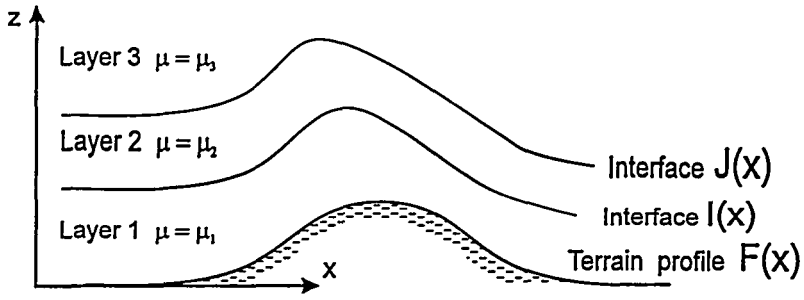

Figure 25. The flow regimes in the model of Carruthers & Choularton (1982).

B Two-dimensional flow model

Carruthers & Choularton (1982) present a model for stably stratified flow over a two-dimensional ridge. The starting point is a vorticity equation

$$\nabla^2\zeta + \mu^2\zeta = 0 \qquad \text{with} \qquad \mu^2 = \frac{g(\frac{d\theta}{dz})_0}{u_0^2\theta}$$

where ζ is the vertical displacement of the streamlines, $(d\theta/dz)_0$ is the upstream potential temperature gradient, u_0 is the undisturbed constant upstream velocity and μ is the stability parameter. Atmospheric stability is simplified to three layers: a surface layer with zero stability, an inversion zone with strong stability and an upper layer with moderate stability. The lowest streamline follows the terrain and streamlines displacements are required to be continuous at interfaces between adjacent layers.

The basic equation is Fourrier transformed to

$$\nabla^2\tilde{\zeta} + (\mu^2 - k^2)\tilde{\zeta} = 0$$

which has solutions of the type

$$\tilde{\zeta}_j = A_j \exp(-\lambda_j z) + B_j \exp(\lambda_j z)$$

with amplitude coefficients A_j and B_j and a vertical scale parameter λ_j. The latter has the following dependence on wave number k and stability μ:

$$-\lambda_j = \begin{cases} -i\sqrt{\mu_j^2 - k^2} & \text{for} \quad \mu_j^2 > k^2 \\ \sqrt{k^2 - \mu_j^2} & \text{for} \quad \mu_j^2 < k^2 \end{cases}$$

The continuity requirements lead to the following equations

$$\begin{bmatrix} e^{-\lambda_1 f} & e^{\lambda_1 f} & 0 & 0 & 0 \\ e^{-\lambda_1 I} & e^{\lambda_1 I} & -e^{-\lambda_2 I} & -e^{\lambda_2 I} & 0 \\ -\lambda_1 e^{-\lambda_1 I} & \lambda_1 e^{\lambda_1 I} & \lambda_2 e^{-\lambda_2 I} & -\lambda_2 e^{\lambda_2 I} & 0 \\ 0 & 0 & e^{-\lambda_2 J} & e^{\lambda_2 J} & -e^{-\lambda_3 I} \\ 0 & 0 & -\lambda_2 e^{-\lambda_2 J} & \lambda_2 e^{\lambda_2 J} & \lambda_3 e^{-\lambda_3 J} \end{bmatrix} \begin{bmatrix} A_1 \\ B_1 \\ A_2 \\ B_2 \\ A_3 \end{bmatrix} = \begin{bmatrix} \tilde{f} \\ 0 \\ 0 \\ 0 \\ 0 \end{bmatrix}$$

where $A_j(x)$, $B_j(x)$, $f(x)$, $I(x)$ and $J(x)$ depend on horizontal distance and $\tilde{f}(k)$ and $\lambda_j(k)$ are wave-number dependent. Carruthers & Choularton (1982) find a computationally efficient scheme for the A_j and B_j amplitudes which determine $\tilde{\zeta}_j(k)$, and the streamline displacements $\zeta(z)$ are found by inverse Fourrier transformation. The model describes many relevant flow phenomena like speed-up at the summit, downdraughts and leeward waves.

C Overview during intensive runs

The following tables contain overview of ground-based observations and radiosonde profiles. The four ground-based stations in the tables are Punta del Hidalgo (H), Piedra del Sueno (S), El Bailadero (B) and Paiva (P) – or the coastal, upslope, summit and downslope sites. The radiosonde profiles are potential temperature θ (circles), wind speed (triangles), wind direction (squares) and water content (diamonds). A two-kink profile is fitted to the lowest part of the potential temperature profile.

		Speed	Dir.	Temp.	R.H.
H	↙	4.9m/s	43±11°	21.1°C	79%
S	↓	3.5m/s	334±14°	18.4°C	98%
B	↓	13.6m/s	337±7°	15.4°C	97%
P	↓	9.7m/s	306±14°	16.5°C	94%

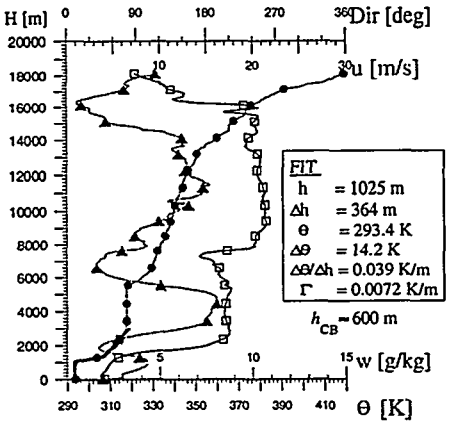

Figure 26. Punta de Hidalgo, June 8 1997, 06 UTC (Run no 2).

		Speed	Dir.	Temp.	R.H.
H	↙	6.2m/s	38±7°	20.8°C	77%
S	↓	5.8m/s	316±14°	18.3°C	92%
B	↓	16.6m/s	334±4°	14.8°C	94%
P	↗	4.5m/s	213±28°	16.3°C	89%

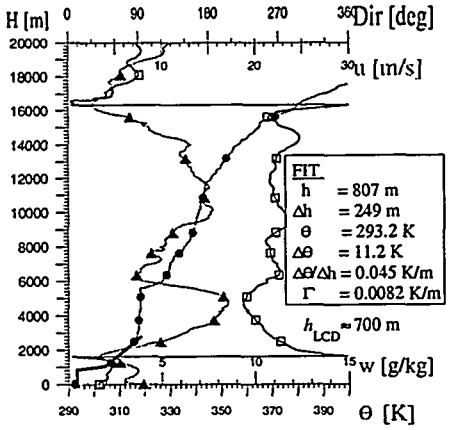

Figure 27. Punta de Hidalgo, June 9 1997, 06 UTC (Run no 3). As figure 26.

		Speed	Dir.	Temp.	R.H.
H	⇗	0.9m/s	221±42°	22.7°C	70%
S	⇓	5.1m/s	302±18°	19.0°C	97%
B	⇓	10.1m/s	338±9°	15.9°C	98%
P	⇑	3.3m/s	166±19°	17.3°C	93%

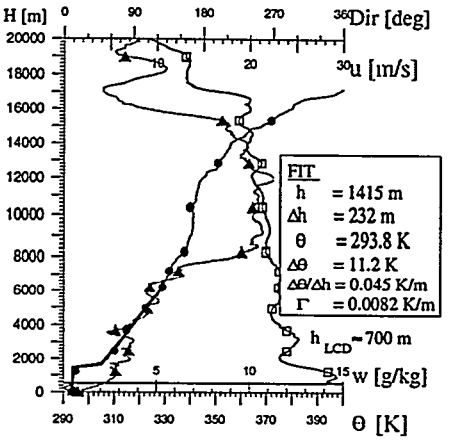

Figure 28. Punta de Hidalgo, June 13 1997, 00 UTC (Run no 4). As figure 26.

		Speed	Dir.	Temp.	R.H.
H	⇙	5.7m/s	32±16°	21.4°C	77%
S	⇓	6.0m/s	306±19°	18.1°C	90%
B	⇓	11.5m/s	333±7°	14.7°C	92%
P	⇑	3.8m/s	165±21°	16.2°C	88%

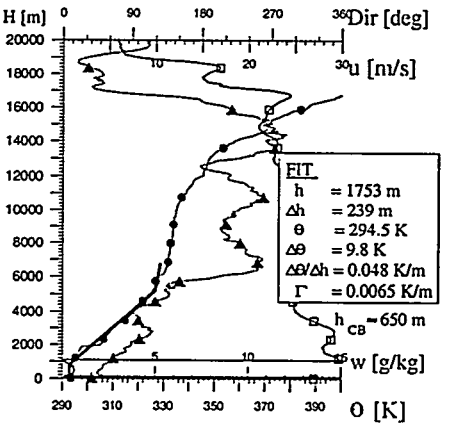

Figure 29. Punta de Hidalgo, June 14 1997, 00 UTC (Run no 5). As figure 26.

		Speed	Dir.	Temp.	R.H.
H	⇙	5.3m/s	40±9°	21.5°C	76%
S	⇓	4.0m/s	303±13°	19.1°C	97%
B	⇓	11.7m/s	331±10°	16.0°C	97%
P	⇗	5.3m/s	237±49°	17.2°C	94%

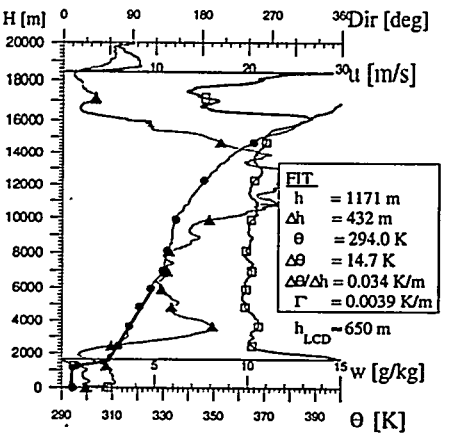

Figure 30. Punta de Hidalgo, June 17 1997, 00 UTC (Run no 6). As figure 26.